Dynamically Supported Geoid Highs over Hotspots: Observation and Theory

Mark A. Richards[1,3], *Bradford H. Hager*[1],

and Norman H. Sleep[2]

1. Seismological Laboratory

California Institute of Technology

Pasadena, California 91125

2. Department of Geology and Geophysics

Stanford University

Stanford, California

3. now at: Research School of Earth Sciences

Australian National University

Canberra, Australia

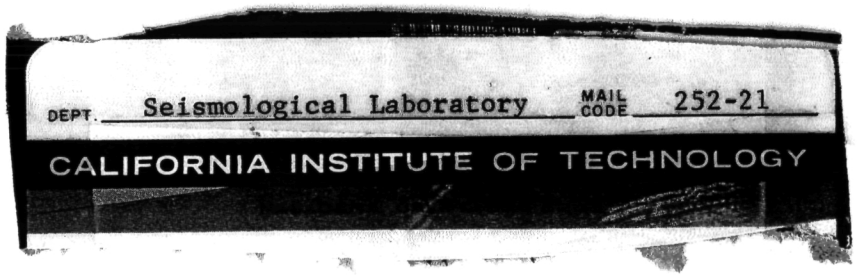

Abstract:

Hotspots are associated with long-wavelength geoid highs, an association that is even stronger when the geoid highs associated with subduction zones are removed. We quantify these associations by expanding the hotspot distribution in spherical harmonics and calculating correlation coefficients as a function of harmonic degree. The hotspot distribution spectrum is essentially white, with peaks at degrees 2 and 6. It is correlated positively with the slab residual geoid for degrees 2-6, with low seismic velocity in the lower mantle at degree 2, and with low seismic velocity in the upper mantle at degree 6. We test a variety of fluid mechanical models for hotspots, including lithospheric delamination and hot plumes, by calculating their predicted dynamic geoid responses and comparing them to the observations. These models include the effects of temperature dependent rheology. Our preferred hotspot model, based on observations of the geoid and seismic tomography, has plumes preferentially occurring in regions of large-scale background temperature highs in a mantle with substantial viscosity increase with depth, although other models are possible. The effect of a relatively low viscosity asthenosphere is to have plumes neck down and attenuate there. The major mass anomalies causing the geoid highs associated with plumes appear to be in the lower mantle.

Introduction:

Linear seamount and island chains, such as the Hawaiian islands, have frequently been attributed to the passage of the lithosphere over deep convective upwellings (Wilson, 1963; Morgan, 1972; 1981). The age progression from the active "hotspot" to the guyots on the inactive end of the chain is particularly well

established for Hawaii (Jarrard and Clague, 1977; Dalrymple and Clague, 1976), and relative motion among the more prominent of these "hotspots" is constrained to be about an order of magnitude less than typical plate rates (Morgan, 1972; 1981; Engebretson et al., 1984; Chase, 1984). Therefore, the thermal plumes, or whatever process is responsible for hotspots, must be essentially stationary with respect to tectonic plate motions.

The hypothesis of mantle plumes has not received universal acceptance, partly because much mid-plate volcanic activity is not easily associated with hotspot traces. For example, the Tertiary volcanic activity in eastern Australia (Pilger, 1982) and the recent volcanism near Easter Island (Bonatti et al., 1977) are actually "hot lines" rather than hot spot tracks. The Line Islands require either widespread contemporaneous volcanism or several hot spot tracks (Schlanger et al., 1984; Epp, 1984b). Alternative explanations for mid-plate volcanism have usually involved propagating cracks or faults in the lithosphere (Betz and Hess, 1942; Turcotte and Oxburgh, 1973; 1976; Sleep, 1974; 1984a; Solomon and Sleep, 1974), even though there is no resemblance between the surface morphologies of mid-oceanic swells and other tensional features in the lithosphere such as mid-ocean ridges and continental rifts.

The crack theory and the plume theory predict very different sub-lithospheric structures beneath a hot spot. These differences can be inferred by considering mid-plate swells such as the one associated with the Hawaiian Islands. These $\sim$1000 km wide features are attributed to heating of the lower lithosphere as it passes over the hotspot (Detrick and Crough, 1978; Crough, 1978; Von Herzen et al., 1982; Epp, 1984a). The topographic uplift appears to form within a few million years at the hotspot and then subside in a manner similar to young seafloor. The thermal origin

(within the lithosphere) of the swells is further indicated by their elevated heat flow (Von Herzen et al., 1982) and the systematics of volcano heights (Epp, 1984a). The formation of the hotspot swells is sufficiently rapid that bulk replacement of the lower lithosphere, as opposed to thermal conduction, is required (Detrick and Crough, 1978). The replacement process could be intrusion of hot plume material into the lower lithosphere or, in the crack theory, bulk stoping or delamination of the lower lithosphere which then sinks as dense blobs into the underlying mantle. The two hypotheses therefore predict opposite types of structures deep beneath hotspots: a hot, low density plume or cold, sinking lithospheric material.

Cases intermediate between these end members are conceivable, and it is necessary to clarify our terminology. By "plumes" we mean more or less cylindrical zones of upwelling with radii of the order of 10-100 km. Plumes might either be strong and supply the bulk of the heat needed to thin the lithosphere, or they might be weaker and act mainly as a trigger for delamination. Broad zones of mantle upwelling are distinguished from narrow plumes. Mostly passive "blobs" in the upper mantle (Allegre et al., 1984; Batiza et al., 1984) which may cause chemical and isotopic anomalies in off-axis volcanism are also distinct from active plumes. We use the term "delamination" to describe either thermally or mechanically triggered sinking of blobs of high viscosity material at the base of the lithosphere, i.e., convective instability. We distinguish this process from lithospheric thinning due only to thermal erosion of the lithosphere by a plume.

Geophysical methods that might discriminate among these alternatives include modelling the gravity signatures of hotspot traces and studies of the deep seismic velocity structure beneath active hotspots. Seismic evidence would seem to favor the

plume hypothesis since certain hotspots such as Yellowstone are underlain by slow velocity material to a considerable depth below the lithosphere (Iyer, 1975; Hadley et al., 1976). Short-wavelength ($<$1000 km) gravity anomalies, although conspicuous, are largely the result of lithospheric thinning and compensated swell topography (Detrick and Crough, 1978; McNutt, 1984) and do not offer much direct information concerning dynamic processes deep in the mantle. However, very long-wavelength geoid anomalies (harmonic degrees $<$10) are relatively insensitive to contamination from lithospheric heterogeneity (Hager, 1983) and are most sensitive to the deep-seated density contrasts in the mantle (Richards and Hager, 1984, henceforth referred to as "RH") that are presumably the result of convection.

The general association of hotspots with long-wavelength geoid highs both globally (Crough and Jurdy, 1980; Chase, 1979) and more locally (Kaula, 1970; Morgan, 1972) suggests that, if hot plumes cause hotspots, topographic compensation dominates their geoid signature; otherwise, low density material would result in geoid lows. Paradoxically, subducted slabs representing cold, sinking material in the upper mantle are also associated with geoid highs (Kaula, 1970; Chase, 1979; Crough and Jurdy, 1980; Hager, 1984), indicating that dynamic surface topography is not the overwhelming effect there. Kaula (1970) explained this apparent contradiction as the result of differing rheology under hotspots and subduction zones. The effect of subducting slabs encountering a relatively high viscosity lower mantle would be to reduce the resulting surface topography ("trench") at long-wavelengths so that the positive geoid anomaly due to the dense slab dominates the geoid signature (Hager, 1984). Thus a conceivable alternative explanation for the geoid highs over hotspots is that cold, dense lithospheric blobs are delaminated at hotspots, resulting in geoid highs

just as do subducting slabs.

The purpose of this study is to provide a test of the various hotspot theories by modelling the long-wavelength geoid anomalies with which they are associated. We use models of hot plumes and cold downwellings (slabs), which include temperature dependent rheology, to predict long-wavelength geoid anomalies which can then be compared with observations. We also consider other quantities of interest such as heat flow and long-wavelength dynamic topography, but they are more difficult to constrain via observation. A key question which we state now and expand upon later is: Could narrow mantle plumes be directly responsible for the geoid highs over hotspots, or are hotspots and, perhaps, plumes associated with more broad-scale temperature anomalies in the mantle which cause geoid highs? Emphasis in modelling will be placed on the conspicuous geoid high over Hawaii since it is the classic hotspot. However, in order to provide a more general observational base, we begin by analyzing quantitatively the relationship between hotspots and the geoid in a global sense, including information from recent seismic studies of mantle heterogeneity.

Global Observations and Hotspots

The Earth's long-wavelength geoid (shown in Figure 1a referred to the hydrostatic figure) has been well determined from observations of satellite orbits (Kaula, 1963; Lerch et al., 1983), but its interpretation has remained somewhat enigmatic because of its lack of resemblance to surface features such as continents and mid-ocean ridges. However, by filtering out the lowest harmonics (degrees 2-3) which dominate the geoid spectrum (see Figure 2), it is obvious that many of the "intermediate" wavelength geoid highs are located over active subduction zones (Figure 1b). This

subduction signal can be removed from the geoid with moderate confidence because of the high degree of formal correlation between slabs and the geoid at harmonic degrees 4-9 (see Figure 3). Hager (1984) has presented a model, which we review in more detail below, that allows us to subtract a subduction geoid signal, calculated using a fluid dynamical model, from the observed geoid to obtain the residual geoid shown in Figure 1c.

The residual geoid is dominated by two large highs centered over Africa - north Atlantic and over the west-central Pacific. Crough and Jurdy (1980) and Chase(1979) recognized that residual geoid highs (left after subtracting slab effects) cover areas that include most of the world's hotspots (marked with dots in Figure 1). Although not as striking as with all degrees included, upon filtering the lowest degree (2-3) components (Figure 1d) we still find more "local" residual geoid highs over many of the hotspot provinces including Hawaii, Tasmania, Raton - Yellowstone - Bowie - Juan de Fuca, Christmas Island - Kerguelen - Crozet - Vema, Afar, Easter - Juan Fernandez, and Iceland - Madeira - Canary - Azores - Cape Verde - Rio Grande - Fernando. The Hawaiian anomaly is very striking and less likely than, e.g., Iceland to be contaminated by plate boundary effects. There are conspicuous exceptions including Mt. Erebus, Samoa, and Bermuda which occur in pronounced residual geoid lows. Also, geoid highs remain over the Iranian-Caucasus-Tibetan highlands, which are related to convergence and thickening of the continental crust (Hager, 1983).

We have selected our list of 47 hotspots (Table I) based on the compilations of Morgan (1981) and Crough and Jurdy (1980). Although exception may be taken with any of several inclusions or deletions (conceivably, only some hotspots are associated with plumes), this list probably represents the distribution fairly well. The

compilation by Burke and Wilson (1976) of 115 possible hotspots also exhibits a strong association with the low-degree geoid as shown by Crough and Jurdy (1980).

The dynamic geoid response of the Earth to internal density contrasts depends quite strongly on the wavelength considered (RH). It is convenient, as well as instructive, to calculate models for comparison to observations in the spectral domain using spherical harmonics. The spherical harmonic representation of hotspots which we use for statistical correlations is obtained by mathematically representing hotspots as point sources of equal (and arbitrary) strength on the surface of the Earth. We have made no attempt to selectively weight certain hotspots such as Hawaii, Iceland, and Kerguelen, which are surely more important than others, such as Raton, whose legitimacy as hotspots may be questioned.

The hotspot distribution spectrum is shown in Figure 2 along with the geoid and slab residual geoid spectra. These spectral amplitude plots are obtained from the square root of the sum of squares of harmonic coefficients at each harmonic degree l:

$$A(l) = \sqrt{\sum_{m=0}^{l} (c_{lm}^2 + s_{lm}^2)/(2l+1)} \qquad (1)$$

The c_{lm} and s_{lm} are the cosine and sine coefficients for a fully normalized spherical harmonic expansion. The factor $1/(2l+1)$ is included because a random distribution of delta functions (hotspots) on a sphere will have a flat ("white") spectrum with this normalization. The hotspot spectrum (Figure 2) is much whiter than either of the geoid spectra; it is mildly peaked at degrees 1-2 with a striking peak also at degree 6. (Because the geoid is referred to the center of mass coordinate system, it has no degree 1 component.)

The correlation coefficient, r_l, between the geoid and hotspots may be obtained from

$$r_l = \frac{\sum_m (c_{lm}\, g_{lm} + s_{lm}\, h_{lm})}{\sqrt{\sum_{m=0}^{l} (c_{lm}^2 + s_{lm}^2)}\sqrt{\sum_{m=0}^{l} (g_{lm}^2 + h_{lm}^2)}} \qquad (2)$$

where (c_{lm}, s_{lm}) are the geoid coefficients and (g_{lm}, h_{lm}) are the hotspot coefficients. Cumulative correlations with several or many harmonic degrees simultaneously can be misleading since spectral power is not uniform (Eckhardt, 1984), so we examine only degree-by-degree correlations. Hotspots are significantly correlated with the observed geoid only at degree 2, but the low-degree correlations for hotspots vs. the slab residual geoid are higher as shown in Figure 3. Confidence limit contours determined by a Student's t test with $2l$ degrees of freedom are also shown in Figure 3. A confidence level of 0.95 implies that there is a 5% probability that the two sets of functions are random.

The residual geoid is significantly correlated with hotspots at degrees 2, 4, and 6 with some correlation at degree 3. Higher harmonics are essentially uncorrelated (no correlations are significant with >90% confidence for l=7–20). The correlations at degrees 2 and 6 are particularly noteworthy because they correspond to peaks in the hotspot spectrum. Crough and Jurdy (1980) found a correlation coefficient of 0.85 at degree 2, significant with >95% confidence, that is even higher than our value of 0.75; the difference arises from different methods of estimating the slab effects.

The degree 2 correlation is made even more compelling by recent observations of seismic velocity heterogeneity in the lower mantle. Both the tomographic inversions of Clayton and Comer (1983) and the least-squares inversion of Dziewonski (1984) of P-

wave travel times show that low velocity in the lower mantle is very strongly correlated with low-degree (2-3) geoid highs (Hager et al, 1985). We also find that slow velocity and presumably hot, low density anomalies are well correlated with the hotspot distribution at degree 2 (r_2=0.85). Figure 4 emphasizes this point by comparing harmonic degree 2 maps of the slab residual geoid, a depth average of seismic heterogeneity from Clayton and Comer (1983), and the hotspot distribution. All of these fields closely resemble the entire low-degree residual geoid (Figure 1c) because the geoid spectrum is so strongly peaked at degree 2. (The vertically averaged lower mantle P-wave velocity model is also peaked at degree 2 as shown in Figure 2.) These three phenomena are apparently related, and even though statistical correlations contain no information concerning cause-and-effect relationships, we form the following hypotheses: 1) The largest residual geoid highs are the result of long-wavelength topographic highs that are dynamically supported by either broad scale or plumelike thermal anomalies; and 2) occurrences of hotspots (mantle plumes) are directly related to the broad-scale temperature structure of the lower mantle. That is, mantle plumes penetrating to the surface to form hotspots are preferentially located in regions of hotter than average mantle. The second hypothesis is suggested in part because the velocity anomaly spectrum inferred from tomography is redder than the hotspot spectrum.

Additional evidence comes from studies of upper mantle heterogeneity from surface wave studies (Masters et al, 1982; Woodhouse and Dziewonski, 1984; Nataf, Nakanishi, and Anderson, 1984; Tanimoto, 1986). At degree 2, there is a high velocity feature in some models of the transition zone that correlates well with the geoid (e.g., Masters et al., 1982; Woodhouse and Dziewonski, 1984; Nataf et al., 1986). This

feature is even better correlated with subducted slabs than with the observed geoid (Hager, 1984; Richards and Hager, 1986) and appears to be associated with cold downwellings rather than hot plumes. Both the Woodhouse and Dziewonski and the Tanimoto studies show a remarkable correlation with both the residual geoid and hotspots at degree 6. Table II gives the degree 6 correlation coefficients, and the negative signs indicate that slow shear velocity is correlated with both geoid highs and hotspots. Since there is a spectral peak in the hotspot distribution at degree 6, the correlation at degree 6 is expected if hotspots are to show a strong relationship to either the geoid or shear velocity anomalies. If the upper mantle is near the solidus, then shear waves could be very sensitive to elevated temperature. In Figure 5 we compare the degree 6 surface wave velocity heterogeneity, residual geoid, and hotspot distributions to illustrate the strength of an $\sim$0.7 correlation coefficient at degree 6. (We should note that the lower mantle heterogeneity models do not correlate significantly with either hotspots or the geoid at harmonic degrees $>$4. Lack of resolution may be at fault. Also note that degree 6 is the one harmonic degree for which slabs do not correlate well with the observed geoid. However, it is only when the dynamically modelled degree 6 slab geoid is removed that the hotspot distribution shows good correlation with the geoid.) Figure 5 shows that the degree 6 hotspot peak represents the large groupings of hotspots (e.g., Christmas Island - Kerguelen - Crozet - Vema) rather than individual spacings which appear to be random. (The hotspot spectrum beyond degree 10 is essentially white.) Again, we can formulate a testable hypothesis concerning hotspots: Plumes are directly related to either heating or chemical heterogeneity in the upper mantle at degree 6, which may be a dominant wavelength for their formation.

These observations suggest that we formulate a quantitative global test to determine whether mantle plumes might be directly responsible for the density contrasts that cause the large-scale residual geoid features as well as the seismic velocity anomalies. The question then becomes that of whether reasonable models of hotspots, either mantle plumes or delaminating lithosphere, can explain the slab residual geoid. The alternative, of course, is that hotspots are only symptoms of a broad-scale thermal field or, perhaps, compositional heterogeneity in the mantle.

The correlations of Figure 3 suggest to us that much of the long-wavelength slab residual geoid is causally related to hotspots. We assume that for each harmonic degree this relationship can be written in the linear form

$$residual\ geoid = (dynamic\ response) * (hotspot\ distribution) + (noise)$$

or, for example,

$$(c_{lm}, s_{lm}) = b_l (g_{lm}, h_{lm}) + (noise) \tag{3}$$

(Note that this assumption is in contradiction of our second hypothesis, which assumes an additional component of heterogeneity, the "long-wavelength background.") From our analysis we obtain the least-squares estimates for the dynamic response functions, b_l, shown in Figure 6. The coefficients (g_{lm}, h_{lm}) are in units of hotspots, and the spectral "response" curve is in the rather peculiar units of geoid/hotspot. Although we cannot reliably determine the response at degree 5, where the correlation is poor, it appears that the response is a relatively smooth, monotonic function of harmonic degree, consistent with a dynamical filtering process as discussed below. Also shown are the values of b_l obtained if, instead of assuming that all the error in estimation is the result of other density heterogeneity signals in

the geoid, we perform the mutual correlation of residual geoid and hotspots under the pessimistic assumption of equal noise in each signal. The extra noise on the geoid (left) side of equation 3 may be due primarily to mismodelling of the subduction signal; at these wavelengths the geoid can otherwise be considered to be perfectly measured. The "equal noise" response is not substantially different than the initial model (equation 3), so our response curve is robust at least in this respect. Unfortunately, the least-squares fits for the coupling coefficients, b_l, are less well constrained as shown by the 2σ error bars at each harmonic degree. The best fitting response amplitudes give about a factor of 8 decrease from harmonic degree 2 to degree 6. This spectral shape is largely that of the residual geoid, since the hotspot spectrum does not show the same long-wavelength bias.

In addition to the global association of hotspots with geoid highs, we can also use the local $\sim$13 m geoid high (degrees 4-10) centered on Hawaii to constrain our models (see Figures 1b,c). The contours are not elongated in the direction of the older islands and seamounts in the chain (toward the northwest), so it is difficult to explain this long-wavelength signal as an effect of the lithospheric swell itself. Intraplate density contrasts do not contribute substantially at these wavelengths (Hager, 1983). The anomaly actually appears to be elongated toward the upstream direction (southeast), suggesting, perhaps, that the active Hawaiian shield is lagging slightly behind a deep thermal source.

The spectral content of the Hawaiian geoid anomaly is difficult to assess quantitatively because it is necessary to arbitrarily select some spatial subdomain within which to perform spectral analysis. However, Figures 7a,b show that about 10 m of the 13 m signal occur in the harmonic degree 4-6 band, while less than $\sim$3 m occur in

the degree 7-12 band. Figure 7c shows that the degree 10-20 geoid signal over Hawaii is almost zero, and also verifies the lack of any consistent correspondence between geoid highs and hotspots (noted above) in this wavelength band. (Note, however, that there is a strong shorter-wavelength signal over Yellowstone.) Since the Hawaiian swell is of relatively small width ($\sim$1000 km), the lack of degree 7-20 signal makes it an implausible source for the longer-wavelength positive geoid anomaly. These observations for the isolated case of Hawaii are consistent with the pronounced long-wavelength bias of the inferred global hotspot geoid response curve of Figure 6. We use both the local and global observations to discriminate among long-wavelength geoid responses for the competing hotspot models discussed below.

Dynamic Response Functions

At this point we review some basic ideas about how long-wavelength geoid anomalies are generated in a viscous, convecting planet like the Earth. Chase and McNutt (1982) and Hager (1983) have shown that only about 20 meters out of a total long-wavelength geoid signal of about 200 meters can be generated by compensated topography and lithospheric or crustal thickness variations, e.g., the geoid high over the Tibetan Plateau. Therefore, most of the geoid must result from the internal density contrasts that drive convective flow: subducted slabs, mantle plumes, or broader scalelength variations.

Interior density contrasts drive flow that causes deformations of the surface, the core-mantle boundary, and possibly, internal chemical boundaries. At very long wavelengths ($l \leq 10$) the lithosphere has effectively no long-term flexural strength (McKenzie and Bowin, 1976), and deformation will occur rapidly compared to the

timescale for convection (RH). These deformed surfaces have an important effect on geoid anomalies. In order to correctly model the long-wavelength geoid, a fluid dynamic Earth model must be used to calculate the geoid contributions due to these boundary deformations. It has been shown by many authors (e.g., Pekeris, 1935; Runcorn, 1964; Morgan, 1965; McKenzie, 1977; Parsons and Daly, 1983; Ricard et al, 1984; RH) that dynamic compensation due to boundary deformation is of dominant importance in determining the geoid. Since induced boundary deformations cause geoid anomalies that are of opposite sign and comparable magnitude to the geoid due to interior density contrasts, long-wavelength geoid anomalies are the difference of large numbers. The details of boundary deformation depend strongly on the viscosity structure of the mantle, so the geoid is a sensitive indicator of mantle structure (RH).

If the viscosity structure varies only radially (i.e., is spherically symmetric), then a given density contrast $\delta\rho_{lm}(r)$ at radius r excites only an lm^{th} harmonic flow field and causes only lm^{th} harmonic boundary deformation. Since solutions for linear (Newtonian), spherically symmetric viscosity may be superposed, we can obtain the total harmonic geopotential coefficients from

$$U_{lm} = \frac{4\pi\gamma R}{2l+1}\int_c^R G_l(r)\delta\rho_{lm}(r)dr \qquad (4)$$

where γ is the gravitational constant, R the Earth's radius, c the core radius, and $G_l(r)$ is the dynamic response function or kernel. This kernel is independent of the azimuthal order m and contains contributions from both boundary deformations and the density contrast itself. In RH we showed how to analytically calculate $G_l(r)$ for spherically symmetric, incompressible, self-gravitating Earth models.

Response functions for both whole mantle flow and chemically layered flow are shown in Figure 8 with lower/upper mantle viscosity ratios of 1, 10, and 100. Note that although flow velocities depend on the absolute value of viscosity, the stresses, boundary deformations, and geoid depend only on the relative values. Free-slip boundary conditions are imposed at the core and at the surface; the difference between no-slip and free-slip is discussed in RH. For uniform viscosity and whole mantle flow (Figure 8a) the geoid response is always negative because of the overwhelming gravitational effect of the deformed upper boundary. Decreasing the viscosity of the upper mantle causes less deformation of the upper boundary (Figure 8b,c) and tends to drive the geoid response toward more positive values. Therefore, both the size and magnitude of the geoid response are strongly affected by relatively mild changes in viscosity with depth. These pressure induced changes can occur either gradually due to compaction or abruptly due to phase changes; phase changes probably do not otherwise strongly affect the flow field (Richter and McKenzie, 1981). However, a chemical discontinuity acting as a barrier to radial flow will deform and also affect the geoid. This forces the geoid response to zero at the boundary (in the same way that we get perfect compensation at the surface and core) and generally reduces the magnitude of the response functions (Figure 8d,e,f).

In addition to the response function $G_l(r)$ we have also calculated dynamic impedance functions, $z_l(r)$ which give the ratio of induced topography to observed geoid (RH). Unfortunately, the Earth's dynamically supported topography is obscured at long-wavelength due to gravitationally compensated continental masses and thermal plate thicknesses, and there is no consistent correlation between topography and gravity. At the present time we cannot reliably estimate the global long-wavelength

(degrees$<$10) dynamic topography associated with mid-oceanic swells or hotspots.

An obvious application of the response functions of Figure 8 is in modelling the subducted slab geoid signal (see Figure 1b). A dynamical model using deep seismicity to locate subducted slabs was developed by Hager (1984). By associating slabs with approximately 0.1 gm/cm ^{3} density contrast and convolving these mass anomalies with various response functions, the following conclusions were reached based on comparison of the observed and predicted geoids: (1) The magnitude and sign of the observed geoid response is consistent with a relatively small degree of dynamic compensation at the surface with most of the dynamic compensation occurring at the core-mantle boundary. (2) The sign of the response function is positive for harmonic degrees 2-9 in the upper mantle, requiring a viscosity increase with depth. (3) Chemically layered models require about a factor of 5 more density contrast associated with subducting slabs than expected. (4) The best-fitting two-layer viscosity model is that of whole mantle flow with a factor of about 30-100 increase in viscosity between the upper and lower mantle (see Figure 8c).

Figures 8b,e,f show that it is possible to have positive responses in the upper mantle and negative ones in the lower mantle for a variety of models. This at first suggests one easy solution to the problem of geoid highs over both slabs and plumes, namely, that the mass anomalies associated with plumes are primarily lower mantle features. (More realistic models that include a low viscosity asthenosphere and high viscosity lithosphere added to model U10 give more positive upper mantle kernels but maintain negative kernels in the lower mantle.) This idea turns out to be basically correct in the numerical plume models which are discussed below. However, we feel that it is important to assess the impact on our response kernels caused by neglecting

the large viscosity variations expected to be associated with slabs and plumes. One motivation for numerical modelling is the hypothesis that these viscosity variations might be responsible for the paradox of having geoid highs over both slabs and plumes.

An alternative explanation is that the geoid highs over hotspots are due to delamination of cold lithosphere, consistent with the slab results. With the upper mantle "calibrated" by the geoid response of cold, subducting slabs, it is straightforward to estimate the geoid signature of unstable lithosphere sinking below a hotspot if we can estimate the amount of high density material present. We present both types of models in the following sections.

Delaminated Blobs

Although the uppermost 30 km of the lithosphere under Hawaii behaves elastically (e.g., Watts, 1978), the portion of the thermal lithosphere below the elastic layer should behave as a cold, dense, high viscosity boundary layer. It is convectively unstable and might sink into the mantle, or "delaminate." For Hawaii, if all of the swell topography is attributed to delamination, the flux of delaminated blobs is comparable to that of slabs at subduction zones. The age of the crust around Hawaii is about 90 Myr and the apparent thermal age after the $\sim$ 1 km uplift of the swell is around 25 Myr (Epp, 1984a). The elevation and hence the average mass anomaly in the lithosphere is proportional to the square root of age, so the delamination is equivalent to subduction of a 20 Myr plate at the rate of hot spot migration (100 mm/yr) across the $\sim$1000 km width of the swell. We assume that large-scale horizontal motions in the mantle are much less than plate velocities (e.g., Hager and

O'Connell, 1979), so that the locus of delamination is roughly fixed with respect to the mantle, not the plates. If we assume 10 Myr as a characteristic time of transit through the upper mantle, then, for a slab of material 1000 km long (along swell) by 1000 km wide with an excess mass per unit area of $3.3x\,10^6$ kg/m ^{2} (associated with the uplift of the swell), the excess mass of lithospheric material in the mantle beneath Hawaii is $\sim 3x\,10^{18}$ kg.

This load can be convolved with the preferred geoid response curves ("U100") for subducted slabs (Figure 8c) to estimate the long-wavelength geoid. If the excess mass is roughly distributed in a cylinder $<$1000 km in radius and 1000 km deep beneath Hawaii, we predict about an 6.3 m geoid high over Hawaii for harmonic degrees 4-9, which is about half the observed signal. However, the spectral response for this model is not nearly as strongly peaked at the lowest degrees as the global response curve (see Figure 18 for a comparison) owing to the small horizontal scale of the load. The degree 2-10 topographic downwarp is about 85 m, a value not likely to be resolved by analysis of bathymetric data given other perturbing influences. The lithospheric swell itself will generate relatively little geoid signal since it is isostatically compensated at shallow depth; whatever signal is generated will also be essentially "white" at low harmonic degrees since the swell is only $\sim$1000 km wide.

The shorter wavelength ($l>10$) geoid contribution could be as much as 10 m if there is little compensation, but this value depends strongly on the detailed viscosity structure of the upper mantle (RH). It is evident that the short-wavelength geoid is not elevated 10 m near the hotspot, and about 300-400 m of downwarp is required to keep the $l \geq 10$ geoid anomaly small. If this downwarp occurs, a place on the seafloor would be expected to experience subsidence (superimposed on the lithospheric swell

due to delamination) as it approached the hotspot, and then uplift as it drifted further west. Since we cannot predict the detailed timing of the delamination it is difficult to model the upstream (east) side of the hotspot. On the west side of Hawaii, simple thermal contraction should produce about 350 m of downwarp in the first 11 Myr if the lithosphere is reset to a thermal age of 25 Myr. If this downwarp is superimposed on an uplift of ~300-400 m due to rebound as the lithosphere moves away from the sinking, delaminated blobs, we obtain approximately a neutral net uplift/subsidence on the downstream side of the hotspot. Although this computation is crude, this might explain the fact that the Hawaiian swell has not substantially subsided as far as 10^0 West of the hotspot as shown in Figure 9. (This topographic variation could conceivably be attributed to greater activity of the hotspot 11 Myr ago.) This description of swell topography due to delamination can be contrasted with the following model based on heat flux from a mantle plume.

Plume Kinematics

Before describing our numerical plume models, we consider a simplified kinematic description of a plume for Hawaii that relates the heat flow, mass flux, temperature excess, and swell topography. Assuming for now that there is no triggered lithospheric delamination, the plume must diverge widely enough beneath the lithosphere to account for the swell width and must also supply enough heat to thin the lithosphere. That is, the flux of positive buoyancy from the plume should equal the rate of production of positive buoyancy in the swell. Using, as before, a migration rate of 100 mm/yr, a width of 1000 km, an elevation of 1 km and a density of 3300 kg/m ^{3} for the swell, the net flux $\dot{m}$ of negative buoyancy is 10 Mg/sec. The actual

mass flux in the plume is the buoyancy flux divided by the fractional density contrast in the plume, $\dot{m}\,\rho/\delta\rho$. For thermal expansion the density contrast is $\delta\rho=\rho\alpha\Delta T$, where ΔT is the excess plume temperature and α is the volume thermal expansion coefficient, $3x\,10^{-5}/^{0}$K. The resulting heat flux from the Hawaii hotspot, $C\dot{m}/\alpha$, ($C=1.2x\,10^{3}$ J/kg ^{0}K is the specific heat) is $4.2x\,10^{11}$ W or about 1% of the global mantle heat flux. The volume of flow, Q, through the plume necessary to make the swell is inversely proportional to the temperature contrast

$$Q = \dot{m}/\alpha\rho\Delta T \tag{5}$$

(For reference, a plume with $\Delta T=100^{0}$K, 100 km diameter, and $\dot{m}=10$ Mg/sec ascending as a cylindrical plug will have an ascent velocity of 4 m/yr.)

Next, the flow from the plume must diverge widely enough to produce the observed swell. To a first approximation this flow can be considered to be the superposition of radial flow from the plume through an asthenospheric channel and the horizontal drag produced by the motion of the plate over the hot spot. The vertically averaged velocity in the asthenosphere far away from the center of the plume is

$$\mathbf{v}_{plume} = (Q/2\pi rA)\hat{\mathbf{a}}_r \tag{6}$$

where r is the horizontal distance from the plume, A is the thickness of the asthenosphere, and $\hat{\mathbf{a}}_r$ is a unit radial vector from the hotspot. The vertically averaged velocity in the asthenosphere from drag at the base of the plate is about half the plate velocity if the base of the asthenosphere is moving much more slowly than the overlying plate:

$$\mathbf{v}_a = (Q/2\pi rA)\hat{\mathbf{a}}_r - v_L/2\hat{\mathbf{a}}_x \tag{7}$$

where the x direction is positive upstream from the plume and v_L is the plate

velocity. The upstream stagnation point occurs at $r_s = Q/\pi A v_L$. The stagnation streamline assuming a 100 km asthenosphere thickness is shown for temperature contrasts of 300^0K and 1000^0K (Figure 9) and the flux computed above. The 1000^0K curve is narrower than the swell, but the 300^0K curve is a fairly good fit to the edge of the swell, which extends about 500 km ahead of the hotspot. (The topographic contours for the Hawaiian swell in Figure 9 have been adapted from Schroeder, 1984, who computed the anomalous seafloor topography in the Pacific ocean after corrections were made for isostatic loading, sediment thickness, seafloor age, etc. Note that the islands and seamounts themselves involve many kilometers of topography, but these loads occur at short wavelength and are partially supported by lithospheric flexure, e. g., Watts, 1978.)

The preceeding calculation is crude, but it shows that the swell shape and buoyancy flux are kinematically consistent with a plume delivering several or many hundreds of degrees excess temperature and also with a reasonable limit for the heat flux due to the Hawaii hotspot. (This heat flux is probably at least a factor of 2 or 3 too high for an average hotspot, since 47 hotspots would otherwise account for half of the Earth's entire heat budget.) It remains to be seen whether a mantle plume fitting this surface kinematic model can also satisfy the geoid observations and constraints from convection theory on the thermal structure of plumes. We consider more refined models in the next section.

Fluid Dynamical Models of Plumes

Our basic idea of a plume is that of a narrowly confined, stable, hot upwelling from a deep boundary layer due to bottom heating. The seismic D'' layer at the bottom of the Earth's mantle may be in part the result of heating of the base of the mantle by radioactive, specific or latent heat within the core. Most estimates for the amount of core heat flux are somewhat less than 10% of the total geothermal flux (Gubbins et al, 1979). If there is a plume under Hawaii it is probably less than $\sim$200 km in radius as evidenced by the width of the volcanic trace (Morgan, 1972b). This small dimension is consistent with a very high effective Rayleigh number and the strong temperature dependence of viscosity, as shown by the stability analysis of Yuen and Peltier (1980).

The thermal structure of a plume is dependent upon such unknowns as the rheological laws of the mantle and plume material, the amount of heat being vented, the superadiabatic temperature drop, whether the plume is chemically distinct from the upper mantle, and the possible influence of partial melting. Thus, we do not know the plume structure very well. By contrast, we can make an educated guess as to the thermal structure of a subducted slab or even a delaminated lithospheric blob. Our approach is to address some general questions about plume dynamics and compare the results to the observations and hypotheses discussed above. In particular, we ask: (1) How does the low viscosity of the plume alter the geoid responses derived for purely layered viscosity? (2) Is the thermal buoyancy of a narrow plume consistent with both the observed amplitude of hotspot geoid anomalies and reasonable limits on the amount of heat flow due to a hotspot?

The main difficulty in modelling is the extreme horizontal variations in viscosity expected for thermal plumes. No analytical methods exist to treat this problem in detail, so a numerical solution is required. We need to calculate very long-wavelength ($\sim$10,000 km) stress fields to obtain long-wavelength surface deformation and geoid estimates, but we must also resolve the strong short-wavelength ($\sim$10-100 km) plume structures which drive the flow. The finite element method is well suited to this problem because of the advantage of variable grid size, and a typical grid for our plume models is shown in Figure 10. In all of the calculations that follow we have used 10 km horizontal grid spacing for treating the prescribed buoyancy forces and viscosity variations for both plumes and slabs, thus allowing good resolution of thermal structures as thin as 50 km or less. Much smaller spacings are possible by further packing the element lattice at the origin, but this was not necessary except as a check on solution accuracy. We have also used 20 km vertical spacing in the top 200 km and bottom 100 km of the mantle to properly resolve viscosity changes in the lithosphere/asthenosphere and core-mantle boundary (D'') region. Rotational or reflection symmetry imposed about $r=0$ (r is the radial distance from the plume center) or $x=0$ gives a total effective width of 10,000 km in both cylindrical and Cartesian geometry. (In the cylindrical calculations we assume a free-slip boundary at the outer boundary of the cylinder, $r=d$.) The numerical code is based on a penalty method formulation (Hughes et al., 1979) of the Stokes flow problem (steady, incompressible, very low Reynold's number flow with spatially variable Newtonian rheology). The code handles nonlinear rheology by damped iteration upon the viscosity field.

We are currently limited to numerical solutions in two dimensions (2-D Cartesian or cylindrical geometry with axial symmetry) rather than the spherical geometry for which we earlier showed analytical solutions. The two-dimensional results that follow are represented in the horizontal spatial wavelength domain, just as we represented our spherical, analytical models (Figure 7) in spherical harmonics. In Cartesian coordinates (appropriate for subducted slabs) we have the approximate spatial wavelength equivalence,

$$\lambda_F \approx 2\pi R / \sqrt{l(l+1)}$$

where λ_F is the Fourier transformed spatial wavelength, l is the corresponding spherical harmonic degree and R is the Earth's radius. In cylindrical coordinates (r, z) with no θ dependence, we use the Fourier-Bessel transform of the spatial coordinate r (see Appendix A). Therefore, for axial symmetry (appropriate for plumes) we have the approximate wavelength equivalence,

$$2\pi d / p_n' \approx 2\pi R / \sqrt{l(l+1)}$$

where p_n' is the n^{th} zero of the derivative of the zeroth order Bessel function, $J_0(r)$, and d is the radius of the cylindrical domain. For our numerical grid, d =5000 km and λ_F =10,000 km for Cartesian geometry, so the maximum allowable wavelengths in both cases correspond approximately to spherical harmonic degree 4. (Due to memory limitations, this was the maximum horizontal dimension our computer model could handle with accuracy and still provide high resolution at the center of symmetry.) The first and second "overtones" in both coordinate systems correspond to harmonic degrees 8 and 12, respectively.

We now consider three different cases in which the low viscosity of a plume may affect the geoid signal. The first case is that of hot blobs (such as those investigated experimentally by Olson and Singer, 1985) guided in their ascent by a narrow, pre-established pathway. The upper surface deformation and geoid due to these solitary blobs can be adequately modelled by the analytical theory (RH). Unless the blobs are very closely spaced, i.e., connected, there will not be an effective low viscosity *stress* pathway to the upper surface (or the core-mantle boundary), so induced surface deformations will not be very different from those calculated using the ambient mantle viscosity structure. Their buoyancy will act approximately as point sources, with respect to the long-wavelength flow-stress field, embedded in a high viscosity background (mantle). The particular case of a hot blob impinging on the lithosphere is a special case which we will discuss later. A more closely spaced string of low viscosity hot blobs might behave more like the plume models described next.

The other two plume types with which we are concerned are like the more classical, steady-state structures in which vertical flow is very rapid with respect to mantle flow as a whole and is nearly uniform, with convergence at the bottom toward the plume and divergence at the top. The probable narrowness ($<$200 km) of mantle plumes implies that the zones of flow convergence/divergence will be of equally small dimension (perhaps that of the D'' layer and the asthenosphere); we temporarily ignore these complications. We can envision two end-member classes of these steady-state plumes for which the low plume viscosity may affect the geoid signature. Mantle plumes may be essentially low viscosity "pipes" in which low viscosity rising fluid is contained by the relatively rigid walls (mantle). The other type is more typical of mantle convection models in which the radial excess temperature profile decays

smoothly away from the axis of the plume (e.g., Parmentier et al., 1975; Yuen and Schubert, 1976; Boss and Sacks, 1985). If the plume is not distinct chemically from the surrounding mantle, a long-lived plume should evolve to this latter state as the surrounding mantle is heated conductively and, possibly, by viscous dissipation. We concentrate on this "thermal halo" case in the models that follow, returning to the "pipe" case when a comparison is needed.

The thermal profile for the halo model can be parameterized by a characteristic width, r_0, and by a peak (axial) excess temperature, ΔT_0, which should be essentially independent of depth if the plume rises nearly adiabatically. The temperature profile near the plume axis must satisfy the condition

$$\frac{\partial T}{\partial r} = 0 \quad at \ r = 0 \tag{8}$$

Since most of the flow and transport will occur very near the axis due to temperature softening of the mantle material, the dynamics of the plume is sensitive to the excess temperature profile. In accord with equation 8, in some models we have adopted the form used by Loper and Stacey (1983)

$$\Delta T = \Delta T_0[1-(r/r_0)^2] \tag{9}$$

where ΔT_0 is the peak excess temperature in the plume and r_0 is a characteristic plume radius. More commonly, we modify (9) to include a thermal "halo" surrounding the mobile near axis region by a temperature profile of the form

$$\Delta T = \Delta T_0 \exp[-(r/r_0)^2] \tag{10}$$

where r_0 gives the characteristic thermal width of the plume. Estimated values for ΔT_0 associated with the superadiabatic increase across D'' vary widely up to a

maximum of about 1000^0K (Verhoogen, 1973). This parameter is not well constrained by observation, and we consider a wide range of values in our models.

The density contrast in the plume is given by

$$\delta\rho = -\rho_0 \alpha \Delta T \tag{11}$$

where ρ_0 is the density at the background mantle temperature and α is the volume coefficient of thermal expansion. We have taken ρ_0=5.14 g/cm ^{3} and α=$3x\,10^{-5}/^0$K. The uplift above an inviscid plume is given by $\frac{1}{2}(D\,\delta\rho/\rho_{0)}$, where D is the mantle depth, so a temperature contrast of only 100^0K results in an excessive uplift of 4.3 km. Therefore, viscous drag must limit flow in the plume.

The viscosity of mantle minerals is a strongly decreasing function of temperature, and we have used the exponential form

$$\eta = \eta_0 \exp(-\beta \Delta T / T') \tag{12}$$

which also closely mimics the form used by Loper and Stacey (1983) for a characteristic temperature T' =2300^0K and $\beta \leq 35$. For example, with ΔT =800^0K and β=35, we obtain more than five orders of magnitude viscosity decrease from the colder surrounding mantle to the hot plume axis. Stress-dependent rheology, by diffusing viscous stresses away from the plume, lowers the effective value of β (Christensen, 1984).

Note that for large values of β or ΔT_0 the combination of exponential dependences in expressions 10 and 12 will restrict most of the flow to a very narrow region near the axis, even though most of the thermal buoyancy, or "halo," may lie outside of this region. Expressions 10 and 12 allow us to characterize a wide variety of dynamical behavior by using β, ΔT_0, and r_0 to specify, independently, the maximum

viscosity contrast, the thermal buoyancy, and the characteristic width of the plume. This parameterization could closely match most published temperature and viscosity profiles for plume models.

We calculate geoid response models for a series of plume geometries of increasing complexity illustrated in Figure 11. (Again, in these models, we assume a thermal structure, rather than obtaining a completely dynamically consistent one using a convection code.) In our first model (A) we consider a simple plume of characteristic width r_0=70 km and peak excess temperature 700^{0}K through the entire depth of the mantle. Using expressions 10-12 to specify the load and laterally varying plume viscosity structure, we have calculated the total geoid response by obtaining the induced boundary deformation from a finite element solution. Strictly speaking, the depthwise, wavelength dependent response functions of equation 4 do not exist for laterally varying viscosity; the different spatial wavelengths are mutually coupled. However, we can construct "pseudo response functions" for comparison with analytic kernels by considering all of the geoid at a particular wavelength to be due only to the load component at that wavelength. The depthwise pseudo response functions for a plume with about 4 1/2 orders of magnitude viscosity contrast (β=35) are shown in Figure 12.

In the absence of lateral viscosity variations, the flow and stress fields due to a density contrast of a given spatial wavelength are independent of disturbances at other wavelengths. Two-dimensional geoid response functions similar to G_l in equation 4 can be calculated analytically as a function of spatial wavelength, and the dotted lines in Figure 12 show responses for a uniform mantle at spatial wavelengths corresponding to harmonic degrees 4, 8, and 12. These functions are exactly the same

in Cartesian and cylindrical geometry for a given wavelength (see Appendix A). The response is uniformly negative due to the dominance of boundary deformation, and the curves are similar to those for the U1 model of Figure 8.

The curves for the low viscosity plume are more negative in the upper mantle than for the uniform viscosity case in the upper mantle, but the effect is rather small in comparison to that of depthwise viscosity variation or chemical stratification (Figure 8). One reason for this is that much of the plume buoyancy, or thermal halo, lies outside of the very low viscosity plume core and the resulting change in surface deformation is relatively small. The change that does occur causes the geoid response to become more negative due to enhanced long-wavelength boundary deformation. We note here that changes in the outer radius boundary condition on the cylindrical domain (at $r=d$) from free-slip to rigid have less than a 5% effect upon the geoid calculations. Therefore, the finite cylinder radius probably has less effect than other neglected effects such as the dynamical interaction of plumes. The long-wavelength deformation field is even less sensitive, so it is safe to conclude that the 5000 km maximum radius for the finite element grid is not a severe limitation in these calculations. Extrapolation to a degree 2 wavelength may be more questionable, but in that case the effects of self-gravitation (RH), sphericity, and self-compression (Ricard et al, 1984; Hong and Yuen, 1985) are even more important. The response curves in Figure 12 are truncated at 200 km depth, because the solution accuracy degrades ($>1\%$ error in the $l=4$ surface deformation compared to analytical solutions) for loads above this level.

The narrowness of a single plume gives essentially equal loading at all wavelengths of interest (a spectrally "white" load) so that the relative geoid response

at each wavelength can be obtained by integrating along the response curves. From Figure 12 we see that the low plume viscosity causes enhancement of the shorter wavelength (l=8,12) geoid and surface deformation compared to the longer wavelengths (l=4). The low plume viscosity allows more efficient transfer of the buoyancy forces ("head") in the plume to the upper and lower surfaces, so that the load is effectively closer to these boundaries. The net result is that the low viscosity associated with plumes tends to make the geoid response spectrum more blue.

The geoid responses in Figure 12 are for a particular choice of parameters. To determine the sensitivity to parameter values, we conducted a range of numerical experiments. The magnitude of the effects of β upon the total geoid signature is shown in Figure 13 for a wide range of the parameters β and ΔT_0. (The relative size of this effect also increases with the plume radius as demonstrated for the pipe models in Figure 16.) Our numerical experiments show that for $(\beta \Delta T_0 / T') < 6$ (less that 2 1/2 orders of magnitude viscosity contrast) the geoid signal is enhanced by a relatively modest factor of 20% or less. Unless the temperature dependence of viscosity is much stronger than given by the rather high value of β=35, a plume temperature excess of at least 600–800^{0}K will be required to substantially affect the geoid signature of this type of mantle plume.

The plume radius, r_0=70 km, in the example of model A was chosen so that the amplitude of the long-wavelength geoid signal (l=4,8) would be comparable to that observed over Hawaii (~13 m) for ΔT_0=700^{0}K. The geoid elevation (per ^{0}K temperature contrast) from this halo model with *no* viscosity perturbation (β=0) is (0.72, 0.72, 0.55) m/100^o K for l=(4, 8, 12) scale lengths. These values can be scaled by the cross-sectional area of the plume ($\sim r_0^2$) within a few percent accuracy over

the range 30 km $< r_0 <$ 100 km. The Δgeoid curves of Figure 13 give the geoid signal ($\beta>0$) in excess of the unperturbed signal ($\beta=0$). The size of the geoid anomaly will scale roughly as $\Delta T_0 \, r_0^2$ unless the effects of low viscosity are very large.

In matching the observed geoid signal, we must not exceed the approximate upper limit of $\sim$10 Mg/sec buoyancy flux (see previous section). Figure 14 shows the buoyancy flux, normalized to a background mantle viscosity $\eta_0=10^{21}$Pa-sec, for r_0=70 km plumes with varying ΔT_0 and β. For β=35, ΔT_0=700^{0}K, we obtain $\sim$200 Mg/sec buoyancy flux, so the mantle viscosity must be raised by a factor of 20 to $2x\ 10^{22}$Pa-sec to lower the flux to 10 Mg/sec. (Flow velocities in all of our examples scale inversely as η_0.) Flow in these plume models is limited by viscous drag in the surrounding mantle; the buoyancy flux varies little with depth except very near the top and bottom of the mantle, and the values in Figure 14 are calculated at mid-depth. Figure 15 shows that the buoyancy flux scales linearly with the 4^{th} power of the radius, r_0^4, as expected for flow in a long, narrow conduit.

We now consider a "pipe" model in which the temperature profile is steplike, i.e.,

$$\Delta T = constant\,,\ r < r_0 \qquad (13)$$

$$\Delta T = 0,\ r > r_0$$

Both temperature and viscosity are uniform within the pipe. Figure 16 shows the geoid effect of low viscosity for a suite of pipe models parameterized by the radius, r_0, and by the viscosity contrast relative to the background mantle viscosity. The unperturbed geoid signal (pipe viscosity = 1.0) is (0.63, 0.63, 0.48) m/100^o K for r_0=70 km (almost the same as for the halo model) and scales as $\Delta T \ r_0^2$ as for the halo model.

We get about 10 m of geoid signal for 800^0K excess temperature in the pipe.

Now we ask: How does the pipe model compare to the halo model in perturbing the geoid signal? We begin by locating a pipe model, r_0=70 km, in Figure 16 that gives about the same perturbation ($\sim$30%) to the l=4 geoid signal (see Figure 13) as did halo model A. This requires a viscosity contrast of about a factor of 0.006 within the pipe. The buoyancy flux for the pipe models is mapped in Figure 17 and scales as the square of the excess temperature (buoyancy x force). For a temperature contrast of 800^0K, radius r_0=70 km, and a pipe viscosity contrast of 0.006, we obtain a buoyancy flux of 36 Mg/sec, or about a factor of 3 1/2 more than for the comparable halo model. Therefore, given the restriction on the maximum allowable buoyancy flux and given the requirement for the amplitude of the geoid signal, the pipe model is not as efficient as the halo model in perturbing (increasing) the size of the geoid signal from the uniform viscosity value. Similar comparisons show that this difference between the pipe and halo models persists, to a varying degree, for other plume radii. Also shown for comparison in Figure 17 (dashed lines) are the fluxes calculated analytically for an infinitely long pipe in a rigid mantle, but with the same pipe viscosity and buoyancy forces; i. e., classical Poiselle flow (proportional to the fourth power of the pipe radius). For very low pipe viscosities (.001-.0001 mantle background), the flow in numerical experiments is limited by the finite pipe length. For high pipe viscosity (.1-1.0 mantle background), induced flow in the mantle becomes significant and the flux in numerical experiments is higher than the analytical result.

In the models that follow we find that large perturbations in the geoid signal (e.g., sufficient alone to account for geoid highs over both subducted slabs and hotspots) often require unacceptably large buoyancy fluxes. Therefore, in seeking to

understand the largest effects on the geoid of low plume viscosity, we concentrate on the halo model. As we discussed previously, many of our inferences about mantle viscosity structure are based on our analysis of geoid anomalies associated with subducting slabs (Hager, 1984; Hager and Richards, 1984). Having seen the effects of low viscosity plumes on geoid response curves, it behooves us to address the related problem of how the high viscosity associated with subducted slabs affects these responses. Before presenting more sophisticated models for hot plumes, we investigate the geoid signature for a very simple model of a cold subducting slab.

We model a high viscosity slab by considering (in Cartesian geometry) a 100 km wide slab, density contrast 0.1 g/cm ^{3}, and having two orders of magnitude higher viscosity than the surrounding mantle. The "slab" for this first example extends throughout the depth of the mantle, so this case and the previous plume models might be taken to simulate the rising and falling hot and cold columns in a very high Rayleigh number, bottom heated, whole mantle convection system. The pseudo response curves for the slab model in Figure 12 show that for $l=4$ and 8 as well as for $l=12$ in the upper mantle, the high slab viscosity causes the response to be much less negative (more positive) than for a uniform mantle viscosity. If the background viscosity layering in the mantle gives a "marginal" upper mantle response, perhaps with a zero crossing such as for model U10 (Figure 8b), both slabs and plumes residing entirely in the upper mantle are qualitatively consistent with positive geoid anomalies.

We now repair some of the obvious inadequacies in plume model A. In model B we have added a high viscosity lithosphere, a low viscosity asthenosphere or outlet channel, and a low viscosity D'' layer which simulates the lower boundary layer

feeding the plume (see Figure 11b). The plume parameters are similar to those of model A with ΔT_0=700^{0}K, β=35, and a slightly diminished radius, r_0=60 km. The total resulting buoyancy flux, 11.0 Mg/sec, accounts for the maximum heat flux for Hawaii if the mantle reference viscosity, η_0, is 10^{22} Pa-sec. The peak velocity in the plume is then 2.3 m/yr.

The long-wavelength dynamic topography (l=4,8) for plume model B is about 165 m. The total long-wavelength geoid signature (l=4,8) is 10.9 m, and the degree 4 and 8 responses are plotted along with the estimated global response curve in Figure 18. (The l=4 and l=8 geoid anomalies from the plume calculation are divided by 4 as plotted in Figure 18; in a real Earth the power concentrated at these wavelengths due to the limited radius of the finite element geometry will actually be smeared over an interval of approximately 4 harmonic degrees.) Although we have obtained a geoid amplitude and buoyancy flux compatible with observation, there are three serious problems with this plume model which are very instructive:

(1) The background mantle viscosity of 10^{22} Pa-sec required to keep the buoyancy flux down to a reasonable value is probably too high a viscosity to assign to the *entire* mantle based on post-glacial rebound and rotational data (Peltier, 1981; Yuen et al., 1982). (This viscosity is probably not too high for the lower mantle, and we shall explore this point further in model C.)

(2) The geoid spectrum from model B is much too white (Figure 8). If we sum up contributions for all wavelengths less than 500 km, we get a total geoid signature of 40 m and 2.6 km of dynamic uplift (in addition to the uplift due to lithospheric thinning). Such a model is clearly not acceptable for any hotspot, including Hawaii. Increasing or decreasing the viscosity of the lithosphere in the model does not

substantially alter the large dynamic uplift; it is mainly the result of allowing the outlet of a strong narrow plume to be within 200 km of the surface.

(3) Subducted slabs in the upper mantle part of model B will not give a positive geoid signal, even if we assign the same viscosity to a downgoing slab as to the lithosphere (see Appendix B). In order to get positive upper mantle geoid response curves similar to those in model U100 of Figure 8 (required in order to fit the observed geoid anomalies over subduction zones), the viscosity of the asthenospheric channel must be at least a factor of 10,000 smaller than the underlying mantle, which we find implausible.

Problem (1) in model B can be eliminated by decreasing the average viscosity contrast in the plume by simply lowering β or by simultaneously lowering ΔT_0 while increasing r_0 (in order to conserve the total geoid signal). Problems (2) and (3) are more difficult and are addressed in model C.

We have yet to find a model that can explain the apparent geoid signatures of both slabs and plumes. An obvious way to approach this problem is to start with a reference model whose upper mantle responses are neither strongly negative nor positive. Model C (Figure 11) satisfies this criterion by including a high viscosity lithosphere, a low viscosity zone extending to 400 km depth, a moderate viscosity increase through the transition zone, and a higher viscosity lower mantle. We have also included a low viscosity D'' layer in which the viscosity profile is determined by a temperature gradient of 7^0K/km (β=35) in accord with the boundary layer model of Stacey and Loper (1983). This layer does not significantly affect the lower geoid harmonics or mid-mantle buoyancy flux, but it is included for consistency with the idea of plumes originating at the core-mantle boundary. If there are no lateral viscosity

variations, the response functions for this model (Figure 19, dotted lines) are small and negative in the lower mantle and are small and generally positive in the upper mantle.

To obtain the geoid response for model C we have used the same plume parameters as in models A and B for the lower mantle except for the plume radius, r_0, which we have increased to 100 km to compensate for the generally smaller low-degree response functions. In the two low viscosity upper mantle layers the plume must diminish in radius if the plume buoyancy flux is approximately constant throughout the entire mantle (i.e., steady-state). If we assume that the temperature excess at the plume's center is also constant (both the plume and mantle are adiabatic) and that β does not vary with depth, then the plume radius, r_0, should decrease as the fourth root of the layer viscosity as demonstrated above. A constant flux plume of 100 km radius in the lower mantle should neck down to $\sim$32 km radius in the upper mantle since $\eta \rightarrow \eta_0/100$. Since the plume buoyancy and geoid signature are proportional to r_0^2, the upper mantle plume will contribute relatively little to the total long-wavelength geoid signature. Most of the geoid signal will result from the lower mantle plume. The reduction of width as the plume rises will also be enhanced if a large fraction of the plume partially melts and causes a large decrease in the plume viscosity. For a temperature excess of 300–700^{0}K the plume might encounter the solidus as little as $\sim$1000 km above the core-mantle boundary (Anderson, 1981). Plumes in the upper mantle may only be streamers of melt from more substantial solid state plumes in the lower mantle.

The depthwise pseudo response functions for this plume model are shown in Figure 19. The lighter line in the upper mantle emphasizes that even though the

normalized response is of the same order for the upper and lower mantle, the upper mantle buoyancy multiplying this response (equation 4) is very small by comparison. Again, the response curves are more negative than for the purely layered case, but when integrated through the lower mantle the resulting geoid spectrum is much stronger at the longer wavelengths (l=4) than at shorter wavelengths (l=12). Note that this would be the case *regardless* of whether or not the low viscosity in the plume affects the response (compare the solid and dotted curves of Figure 19). The plume radius of 100 km for this model results in a geoid signature of similar amplitude to the global response curve as shown in Figure 18. The geoid spectrum is now much more "red" (biased toward long-wavelengths) than for our other plume models and is a more satisfactory approximation to the global response spectral shape than any of our previous models. (The total signature for l=4,8 is less than 5 m, so scaling the plume radius up to about r_0=140 km will account for the Hawaiian anomaly.) The short wavelength geoid signature (l>12) is only a few meters, so model C does not suffer the problems of very large geoid anomalies at shorter wavelengths that we found for model B. The shear stress, τ_{rz}, at the base of the lithosphere drops from about 10 bars at a distance of 200 km from the plume center to only about 1 bar at a distance of 1200 km, so the plume will not drive much plate motion. The shear stress at plume center is over 200 bars and might result in erosion of the lithosphere.

The buoyancy flux for model C (r_0=100 km) is 85 Mg/sec for a lower mantle reference viscosity η_0=10^{22}Pa-sec, however, so unless the average viscosity of the lower mantle is as high as 10^{23} Pa-sec, this model must be considered unacceptable. But if we use a weaker temperature dependence for effective viscosity (likely due to stress-dependent effects) or a lower excess plume temperature, we can greatly reduce

the flow while preserving the geoid signature. For example, a reduced value of β=22 produces essentially the same geoid signature as for β=35 with a buoyancy flux of only 10.5 Mg/sec for η_0=10^{22} Pa-sec. Alternatively, for ΔT_0=300^0K and β=35, essentially the same geoid response may be produced by a plume of radius 200 km in the lower mantle and with a buoyancy flux of only 0.52 Mg/sec. A wide range of plume parameters can, therefore, match the geoid and flux constraints either globally or for the particular case of Hawaii.

Both the low viscosity plume geoid response curves and the purely layered viscosity curves (dotted) in Figure 19 will give the correct long-wavelength spectral characteristics for hotspots. The overall negative response functions (resulting in geoid highs for low density plumes) in the lower mantle overwhelm the upper mantle plume signal because the plume's radius is smaller in the low viscosity upper mantle. This necking down effect may be very important to the dynamics of mantle plumes, especially plumes of lower mantle origin, and appears to be a neglected phenomenon in both numerical and experimental modelling.

To emphasize the relative importance of vertical stratification of mantle viscosity, we have included two additional models in the spectral response plot of Figure 18. First, model C ' (β=0) is the same as model C, except that there is no viscosity contrast between the plume and surrounding mantle. Its spectrum is somewhat more "red" than for β=35, and, according to the numerical experiments (model A type) discussed above, this purely layered model is probably sufficiently accurate for up to two orders of magnitude viscosity contrast within the plume. We can also perform this type of calculation (β=0) analytically for *spherical* Earth models including all harmonic degrees. For a 300^0K plume of 200 km radius (no viscosity contrast) in the

model C type layered mantle, we obtain the response given by dashed lines in Figure 18. (The slight differences between this curve and model C′ illustrate the effects of sphericity.) This response curve gives a reasonable, although not optimal, fit, at least for $l \leq 8$, to the observed global response curve. Clearly, increasing mantle viscosity with depth can result in a strong low-degree bias in the geoid signature of a plume (or any convective upwelling or downwelling), regardless of the viscosity of the plume itself. This is one of the main points to be gained from our numerical models.

Our geoid models involve the balance between dynamic surface deformation and the (plume) load. Figure 20 shows the actual radial profiles of surface deformation from models B and C. Shown for comparison are Hawaiian swell profiles A-A′ and B-B′ from Figure 9, which cross the island of Hawaii and a point 500 km "downstream," respectively. Figure 20 shows the relative richness in long-wavelength surface deformation in model C compared to model B. Dashed lines also give the deformation with no viscosity contrast in the plumes (β=0). For our "preferred" model C, the predicted long-wavelength deformation outside of the swell is several hundred meters, which is probably not resolvable from bathymetric anomalies. However, the swell topography itself is not explained by this model. Furthermore, since the ridge-like swell topography extends far toward the WNW from the active hotspot, lithospheric thinning (effectively resetting the thermal age of the lithosphere) is obviously a more satisfactory explanation (Detrick and Crough, 1978). The predicted short-wavelength (<500 km wide) deformation from model C of more than 1 km will be reduced by lithospheric flexure and masked to a great extent by the ~8 km seamount topography (volcanic edifice) itself, which does not appear in Figure 20.

We now have an acceptable working model for a plume derived long-wavelength geoid. The main virtues of model C are that it has a generally negative lower mantle geoid response for $l \leq 8$ and that it involves a substantially reduced upper mantle contribution. We must now determine if this model is compatible with the observed subducted slab geoid response.

Contrary to what we found for model A, for model C, with a 100 km wide slab with the same viscosity as the lithosphere and extending to 1100 km depth, the response (Figure 19, heavy-dashed line) is now more negative than for the purely layered model and produces almost a null geoid signature for slabs at degrees 4 and 8. The slab load is coupled relatively more efficiently to the lithosphere than before, resulting in more surface deformation and a more negative geoid response.

This coupling may not occur in the real Earth since the lithosphere at subduction zones is weaker than normal (e.g., Sleep, 1979; Hager and O'Connell, 1981). If we simulate the weak plate boundary by reducing the effective viscosity of the lithosphere by two orders of magnitude within 100 km of the subducting slab, the slab is supported more by the high viscosity of the lower mantle. This results in less long-wavelength surface deformation and a much more positive response (Figure 19, heavy, dash-dot line).

Comparing the slab-with-weakened-lithosphere response with either the plume response or the purely layered response, we see that it is possible to have geoid highs over both plumes and slabs. This in itself is not too surprising considering the results of model A. However, the detailed rheology of subduction zones is of even more importance than the influence of low plume viscosity. The "calibration" of the upper mantle geoid response using subducted slabs depends strongly on the

parameterization of the lithosphere. Hager's (1984) conclusions, based on a simple two-layer parameterization of rheology, that the slab-geoid observations favor penetration of the 670 km discontinuity by slabs and require a one to two order of magnitude increase in mantle viscosity through the upper mantle are valid, but the details of the upper mantle structure are not well resolved. In Appendix B we have included a more systematic analysis of models for rheological variations associated with subducting slabs. On the basis of these models we conclude that the lithospheric weakening effect is the most efficient way to make the slab geoid response more positive than for purely layered viscosity. A more extensive treatment of the large-scale dynamic support of subducting slabs, including such effects as dip angle and non-linear rheology, might yield important new insights, but such a study is beyond the scope of this paper.

In order to obtain average subducted slab velocities of about 100 mm/yr in model C, it is necessary to set the lower mantle reference viscosity η_0 to 10^{22} Pa-sec. This value, which is substantially higher than recent estimates from post-glacial rebound (Peltier, 1981) and rotational data (Yuen and Sabadini, 1982), served as the reference viscosity in our model C plumes. We can think of two resolutions of this apparent paradox. One is that the rotational response is actually on the high viscosity branch (O'Connell, 1971). The other is that postglacial rebound samples transient rheology while convection responds to steady-state rheology.

Finally, we consider an upper mantle plume for model C, i.e., one that originates above 670 km depth. In order to get the l=4,8 purely layered responses to become negative in the upper mantle, it is necessary to have more than 3 orders of magnitude viscosity contrast in the plume. As before, a plume radius $\geq$70 km is required to

produce the observed geoid anomaly over Hawaii. However, we again obtain too much heat flow (even for an *upper* mantle viscosity as high as 10^{21} Pa-sec) just as we did for plume model B. This problem results from the low viscosity of the plume, and this is the main difference between our calculation and Morgan's (1972) estimate of a 75 km radius upper mantle plume. The plume can only overcome the effects of viscosity stratification (required by slabs) by stronger coupling of buoyancy from the lower parts of the plume to the surface through the low viscosity channel. It is very difficult then to produce large positive geoid anomalies over primarily upper mantle plumes without violating reasonable limits on plume heat flow. Since the conditions under which model C can satisfy the slab observations are somewhat extreme (high viscosity slab and very weak lithosphere), this conclusion is difficult to avoid by contrivances in the upper mantle viscosity structure. This is not to say that strictly upper mantle plumes do not exist, but only that they are an unlikely source of long-wavelength geoid highs.

Larger-scale Plumes in the Upper Mantle?

The final issue we address is that of more broad-scale heating associated with hotspots in the upper mantle, or, perhaps, a solitary blob of hot material impinging on the base of the lithosphere. (The correlation of surface wave velocities with the degree 6 geoid and hotspot expansion may be symptomatic of a hotter than average asthenosphere.) In order to fit the observed long-wavelength bias described above, the basic horizontal scalelength of heating surrounding a hotspot must be $>$5000 km. This will lower the average viscosity of the upper mantle on a scale much larger than the depth of the upper mantle, resulting in geoid response curves that are more

positive, not more negative. In other words, coupling of the buoyancy forces to the lithosphere will be weakened by higher temperature and lower than average viscosity, resulting in less surface deformation. Therefore, given the requirement of increasing upper mantle viscosity with depth (based on slab modelling), we cannot explain geoid highs over such broadscale hot blobs in the uppermost mantle. Again, this does not exclude the existence of hotter than average asthenosphere associated with hotspots (which we would expect at the head of any thermal plume), but our models imply a deeper source for the associated geoid anomalies.

In this same vein, it is curious that the strong correlations of the residual geoid with hotspots at degrees 2 and 4 are not accompanied by significant correlations between hotspots and upper mantle seismic velocity variations (Richards and Hager, 1986). This also suggests a deep source associated with, if not caused by, plumes, and is consistent with the greater sensitivity of the lower geoid harmonics to density heterogeneities at great depth in the mantle. Lastly, we note that the surficial evidence for mantle plumes indicates that they are very narrow, at least in the upper mantle. The Hawaiian swell is only of order 1000 km in width, and the volcanic shields (islands) form a much narrower track within the swell. An active thermal source at the base of the lithosphere an order of magnitude wider seems unlikely.

Discussion

The geoid models we have presented show that there is no inherent contradiction in having geoid highs produced by both subducted slabs in the upper mantle and mantle-wide plumes. If the thermal buoyancy of plumes directly generates the observed geoid highs, we can offer some restrictions on their characteristics:

(1) Plumes that are of uniform strength in terms of thermal buoyancy (approximately constant in radius), or that are primarily upper mantle phenomena, cannot produce the very long-wavelength bias (degrees 2-6) of the observed geoid. They are also unlikely candidates to produce the more local ($l \geq 4$) geoid highs over hotspots.

(2) Plumes that are of radius ~100-200 km ($\Delta T_0 \approx 200$–700^0K) in the lower mantle, but that become much more confined as they rise due to decreasing mantle viscosity, can produce the low-order geoid (degrees 2-6). However, such plumes must be restricted to about 3 orders of magnitude or less viscosity contrast in order not to exceed maximum estimates for heat flux from the core. Much narrower, low viscosity plumes (e.g., Loper and Stacey, 1983) can also account for the heat flux, but they cannot cause the long-wavelength geoid anomalies.

(3) More local, intermediate wavelength ($l \geq 4$) geoid anomalies associated with hotspots may be caused by either the plume itself or triggered lithospheric delamination due to the plume. Unfortunately, this study has not revealed a method based on geoid models to discriminate between these alternatives. It is remarkable that the delamination could indeed cause large (>5 m) geoid anomalies, but this process is not able to produce the low-order (l=2–6) observed geoid without producing much more pronounced and consistent local (l >6) anomalies over hotspots. Of particular importance is the temperature of the sublithospheric upper mantle, which would be heated by plumes but cooled by delaminated blobs. (The mantle at lithospheric depths is heated by both processes.) The strong association of hotspots with both low velocity upper mantle (degree 6) and lower mantle (degree 2) as revealed by seismic studies, along with the relatively stationary nature of hotspots with respect to plate motions, implies that they are at least symptomatic of deep thermal processes. None of these

observations supports passive lithospheric delamination (e.g., due to cracks) as the primary source of either hotspots or the observed geoid.

The correlation of hotspots with low-order residual geoid highs (Figure 1c) and with seismic velocity anomalies (Figure 4) does not necessarily imply that the thermal anomalies within the plumes associated with hotspots are the primary cause of these phenomena. The considerable effort we have made to explore the conditions for which this is possible should not be taken to imply that we necessarily believe in such a strong role for plumes. Even our "preferred" model C appears unsatisfactory in some respects. In order to explain the low-degree (2-3) geoid, nearly all 47 of our selected hotspots would have to be associated with very large plumes (e. g., radius=200 km and average temperature contrast 300^0K), and with conspicous "local" ($l \geq 4$) geoid anomalies. Hawaii and a few other major hotspots might fullfill this prescription, but many others would seem unlikely candidates.

Further insight into this question may be gained from consideration of the global hotspot distribution. Hotspots are distributed almost randomly over about half the Earth's surface (contained by the large residual geoid highs), but are almost absent in the other half of the globe. Stefanic and Jurdy (1984) have claimed less than 1% likelihood that such a broad-scale bimodal pattern is random, and we suspect that the location of hotspots is controlled by some other global thermal pattern in the mantle that limits their surface access to the areas of the large-scale geoid highs. An alternative explanation related to a process of delamination is not evident.

A candidate control mechanism is found by considering the reconstruction of paleo-subduction zones proposed by Chase and Sprowl (1983). If, as they claim, the Pangean supercontinental assemblage was surrounded by subduction zones at $\sim$125

Myr B.P., then the major residual geoid lows (Figure 1c) correspond to areas which have experienced subduction as the American continents have swept westward during the last ~100 Myr. These are also areas largely devoid of hotspots, with some exceptions such as Yellowstone. Intense shearing in the mantle and/or thermal quenching due to deeply subducted material may block or completely shut off mantle plumes. Strong plumes such as Hawaii, Iceland, and Kerguelen have probably been shielded from subduction for 100 Myr or more. Chase and Sprowl also point out that other hotspots such as Mt. Erebus, having only recently escaped a subducting slab, are relatively weak newcomers.

This conceptual model provides an alternative explanation for the correlation of low seismic velocity at very long wavelength in the lower mantle with both the largest geoid highs and hotspots. High seismic velocity in the lower mantle may be giving us a broad-scale map of dead slabs that have been deposited in the lower mantle during the last 100-200 Myr, and these positive mass anomalies, combined with negative lower mantle response kernels, would generate geoid lows. Both Figures 8 and 19 show that this would not be a contradiction of the fact that currently subducting slabs in the upper mantle cause geoid highs. Lower mantle response functions are probably negative even with a low viscosity asthenosphere. We can roughly estimate the degree 2 geoid from ancient subducted slabs in the lower mantle as follows:

Subducted slabs currently residing in the upper mantle cause about +20 m of degree 2 geoid for an average upper mantle response of +0.3 (see Figure 8c). For a purely layered such as used for model C' model we calculate an average lower mantle degree 2 response (using the spherical, analytic model of RH) of about -0.1. If we assume that the ancient subduction zones have put 10 times as much lithosphere into

the lower mantle over the past 100 Myr as currently resides in the upper mantle due to recent subduction, then we estimate ~70 m amplitude degree 2 geoid lows associated with these old subduction zones. This is about the right size to explain the current low-degree geoid. Also, dead slabs in the lower mantle will produce a very attenuated signal at higher harmonic degrees, resulting in a geoid spectrum strongly peaked at degree 2. Further reddening of the geoid would result from shearing and diffusing away of short wavelength slab heterogeneities. Since at least 70% of the Earth's heat flow is involved in the cooling of lithospheric plates (O'Connell and Hager, 1980), this explanation is satisfactory in that the largest geoid features are related to the dominant mode of convection. This scenario, with a relatively passive lower mantle, is similar to the recently proposed whole mantle convection model of Loper (1985), although we have been motivated by different observations. The mantle convecting system, dominated by internal heating and driven by subduction of the upper boundary layer (plates), would be semi-transparent to mantle plumes resulting from a relatively small heat flux from the core. Such plumes could, of course, be much smaller in radius than those required to directly cause the long-wavelength slab residual geoid, which might result from long-wavelength variations in background temperature.

If the Pangean supercontinent was stable for a long period of time, the geoid may have a long-term memory of that episode as proposed by Anderson (1982). A ring of subduction around this supercontinent may also have resulted in antipodal rifting and broad-scale upwelling in the central Pacific which is also "remembered" by a large residual geoid high. Hotspots shielded from subduction beneath the supercontinent would have caused long-term heating beneath the continental lithosphere.

This may have eventually led to the breakup of the stable configuration as evidenced by the many hotspots along the mid-Atlantic ridge and the African continent. Thus, the two convecting systems interacted strongly at this point. The chemically buoyant supercontinent may have stabilized a degree 2 convection mode on Earth of which the present geoid is a fossil, and the correlation of hotspots with the low-degree geoid is symptomatic rather than causal.

This hypothesis stands in contrast to the possible dominant role of hotspots on Mars and Venus. The largest gravity and topography anomalies on Mars are due to the Tharsis bulge (Sleep and Phillips, 1985) which contains huge shield volcanoes. On Venus, the large gravity highs over the highland areas are most easily attributed to large mantle plumes in a relatively isoviscous mantle (Kiefer et al., 1986). A central question that remains, in our view, is that of just which density contrasts in the Earth's mantle cause the large-scale shape of both the geoid and the lower mantle velocity variations. We cannot completely resolve this issue on the basis of our study, even though only a restricted class of hotspot models can account for the geoid. However, because not all hotspots are associated with local geoid highs, even our "preferred" plume model is not a very satisfactory explanation for low-degree (2-3) geoid highs. More broad-scale sources appear to offer a less problematic explanation.

This work might be improved by substituting a variety of fully dynamic convective plume solutions for our generalized plume models. We hope that some of our obvious oversimplifications may spur other workers to predict long-wavelength geoid anomalies from their plume models. Improvement in the resolution of seismic velocity anomalies in the deep mantle can be expected, since this is a relatively recent area of research.

Acknowledgements

This work has been supported by NASA grants NAG 5-315 and NSG-7610 and by a Sloan Foundation Fellowship to Bradford H. Hager. Contribution No. 4336, Division of Geological and Planetary Sciences, California Institute of Technology, Pasadena, California 91125.

Appendix A: Dynamic Geoid Anomalies in Cylindrical Geometry

The governing first-order differential equations for incompressible flow at very low Reynold's number include the continuity condition

$$\nabla.\mathbf{v} = 0$$

the equations of motion

$$\nabla.\tau + \delta\rho\mathbf{g} = 0$$

and the Newtonian constitutive law

$$\tau = -p\,\mathbf{I} + 2\eta\epsilon$$

where $\mathbf{v}$ is the velocity vector, $\mathbf{g}$ the gravitational acceleration, $\delta\rho$ the density contrast, τ the stress tensor, ϵ the strain rate tensor, η the viscosity, p the pressure, and $\mathbf{I}$ the identity matrix. In cylindrical coordinates $(r\,,z\,)$ we have

$$\frac{\partial v_z}{\partial z}+\frac{1}{r}\frac{\partial}{\partial r}(rv_r\,) = 0 \tag{A1}$$

$$\frac{\partial \tau_{rr}}{\partial r}+\frac{\partial \tau_{zr}}{\partial z}+\frac{1}{r}(\tau_{rr}-\tau_{\theta\theta}) = 0 \tag{A2}$$

$$\frac{\partial \tau_{zr}}{\partial r}+\frac{1}{r}\tau_{zr}+\frac{\partial \tau_{zz}}{\partial z} = -\delta\rho g \tag{A3}$$

$$\tau_{zz} = -p + 2\eta \frac{\partial v_z}{\partial z} \tag{A4}$$

$$\tau_{rr} = -p + 2\eta \frac{\partial v_r}{\partial r} \tag{A5}$$

$$\tau_{zr} = \eta \left(\frac{\partial v_r}{\partial z} + \frac{\partial v_z}{\partial r} \right) \tag{A6}$$

$$\tau_{\theta\theta} = -p + 2\eta \frac{v_r}{r} \tag{A7}$$

We can eliminate the r dependence by an appropriate Fourier-Bessel respresentation. For example, for a finite cylinder of radius a the radial velocity must vanish at a, so we can write the inverse discrete transform

$$v_r(r,z) = \sum_{n=1}^{\infty} v_r^n(z) J_1 \left(\frac{p_n' \, r}{a} \right) = F_1^{-1} [v_r^n]$$

where $[v_r^n]$ is the discrete Fourier-Bessel transform of $v_r(r,z)$ and p_n' is the n^{th} zero of the first-order Bessel function J_1. With some foresight concerning the use of orthonormal expansions, and with F_0 respresenting the zeroth order transform, we also write:

$$v_z = F_0^{-1} [v_z^n]$$

$$\tau_{zz} = F_0^{-1} [\tau_{zz}^n]$$

$$\tau_{rz} = F_1^{-1} [\tau_{rz}^n]$$

$$p = F_0^{-1} [p^n]$$

$$\delta\rho = F_0^{-1} [\delta\rho^n]$$

The stresses $\tau_{\theta\theta}$ and τ_{rr} will turn out to be mixtures of J_0 and J_1, but will be

formally eliminated from the equations in a later step.

Some useful orthogonality and completeness properties of Fourier-Bessel transforms are summarized below (see Sneddon, 1951).

Orthogonality:

$$\int_0^a r J_l\left(\frac{p_m r}{a}\right) J_l\left(\frac{p_q r}{a}\right) dr = \begin{bmatrix} \frac{a^2}{a} J_{l+1}^2(p_m),\ m = q \\ 0,\ m \neq q \end{bmatrix}$$

where p_m and p_q can be either the zeros or the zeros of the first derivative of J_l.

Representation (completeness):

$$f(r) = \sum_{m=1}^{\infty} J_l\left(\frac{p_m r}{a}\right) \left[\frac{2}{a^2 J_{l+1}^2(p_m)} \int_0^a f(r) J_l\left(\frac{p_m r}{a}\right) r dr\right.$$

Useful derivatives:

$$\frac{\partial}{\partial r} J_0(kr) = -kJ_1(kr)$$

$$\frac{1}{r}\frac{\partial}{\partial r}\left[rJ_1(kr)\right] = kJ_0(kr)$$

for any real k.

By taking $\int_0^{\infty} rJ_0(kr)$ [eq. (1)] dr and using the expansions for v_z and v_r, we obtain a transformed equation:

$$Dv_z^n + kv_r^n = 0 \qquad \text{(A1')}$$

where $D \equiv \frac{d}{dz}$ and the wavenumber is $k = \frac{p_n'}{a}$. Similarly we obtain for Equations 6 and 3

$$\tau_{zr}^n = \eta(Dv_r^n - kv_z^n) \tag{A6'}$$

$$0 = D\,\tau_{zz}^n + k\,\tau_{rz}^n - \delta\rho^n\, g \tag{A3'}$$

If we use equations 1, 5, 6, and 8 to eliminate $\tau_{rr}-\tau_{\theta\theta}$, $\frac{\partial \tau_{rr}}{\partial r}$, and $\frac{\partial v_z}{\partial z}$ from equation 2, we obtain

$$D\,\tau_{rz}^n = k\,\tau_{zz}^n + 4\eta k^2 v_r^n \tag{A2'}$$

Equations $1'$, $6'$, $3'$, and $2'$ are identical in form to the two-dimensional Cartesian formulation of Cathles (1975) and Hager and O'Connell (1981)

$$D\begin{bmatrix} v_z \\ v_r \\ \tau_{zz} \\ \tau_{zr} \end{bmatrix} = \begin{bmatrix} 0 & -k & 0 & 0 \\ k & 0 & 0 & 1/\eta \\ 0 & 0 & 0 & -k \\ 0 & 4\eta k^2 & k & 0 \end{bmatrix} \begin{bmatrix} v_z \\ v_r \\ \tau_{zz} \\ \tau_{zr} \end{bmatrix} + \begin{bmatrix} 0 \\ 0 \\ \delta\rho g \\ 0 \end{bmatrix} \tag{A8}$$

where we have dropped the wavenumber superscript n . This system of equations can be solved analytically for $\mathbf{v}$ and τ via a propagator matrix technique for arbitrary layering of viscosity with depth (z) (see Hager and O'Connell, 1981, for examples).

Thus the depth dependence for cylindrically symmetric flow in layered media can be solved in exactly the same way as for 2-D Cartesian coordinates. For a prescribed cylindrically symmetric loading problem driven by $\delta\rho\left(\frac{p_n{}'}{a}\right)$ we can write

$$\begin{bmatrix} v_z \\ v_r \\ \tau_{zz} \\ \tau_{zr} \end{bmatrix}_{cylindrical} = \begin{bmatrix} v_z \\ v_x \\ \tau_{zz} \\ \tau_{zx} \end{bmatrix}_{Cartesian}$$

with the Cartesian solution driven by $\delta\rho(k)$, where $k = 2\pi/\lambda$ and λ is the spatial

wavelength, if

$$k = \frac{p_n{}'}{a}$$

In other words, cylindrical and Cartesian flow are "wavenumber equivalent". Note also that in an effectively infinite domain ($a \rightarrow \infty$) we can use the integral transform

$$v_r(r,z) = \int_0^\infty v_r(z,\alpha) J_1(\alpha r) \alpha d\alpha$$

to again obtain equations 8. In practice, we have used the discrete transform to represent our finite element results in the wavenumber domain.

Appendix B: Slab Geoid Models with Variable Viscosity

We have tested two series of models. The first ("L100") has a 100 km thick high viscosity ($100\eta_0$) lithosphere with a uniform background mantle viscosity (η_0). Geoid anomalies are calculated in a box of width 4000 km (corresponding to $l=5$ with reflection symmetry imposed at the left side boundary). The finite element grid is the same one shown in Figure 10. The 100 km thick slab extends to 1100 km depth (Figure B1) and is assigned a density contrast of 0.1 g/cm ^{3}. (The density contrast actually normalizes out of the response curves.) Pseudo response functions are calculated at four depth intervals ranging from 200 to 1100 km depth (accuracy is not sufficient for loads above 200 km) and are plotted in Figure B2 for the first and second harmonics ($l=5,10$) of the box.

Model L100.u (Figure B2, dotted lines) gives the purely layered response. In model L100.slab (solid lines) the slab is assigned viscosity $100\eta_0$. In models L100.slab200 and L100.slab400 (long and short dashes) the lithospheric viscosity is

lowered to η_0 within 200 km and 400 km, respectively, of the center of the downgoing slab. As shown in Figure B2, the effects of these rheological variations are relatively mild. Stronger coupling of the slab load to the lithosphere through the high viscosity slab causes the responses to become more negative in the deeper part of the slab.

The second series of models ("LU100") is the same as the L100 series except that the background viscosity of the lower mantle (below 670 km) is increased to $100\eta_0$. Figure B3 gives the pseudo response curves for models LU100.u, LU100.slab, LU100.slab200, and LU100.slab400 (dotted, solid, long-dashed, and short dashed lines, respectively). Here the effect of decreased lithospheric strength near the slab is more pronounced. The slab is less strongly coupled to the lithosphere and more strongly coupled to the high viscosity lower mantle. This results in less upper surface deformation and gives a much more positive geoid signature for models LU100.slab200 and LU100.slab400. Again, we cannot resolve the geoid anomalies accurately for loads above 200 km depth. However, our parameterization is probably too coarse to represent the subduction process in this complicated zone even if a finer grid spacing were possible.

References

Allegre, C. J., B. Hamelin, and B. Dupre, Statistical analysis of isotopic ratios in MORB: the mantle blob cluster model and the convective regime of the mantle, *Earth Planet. Sci. Lett., 71*, 71-84, 1984.

Anderson, D. L., Chemical plumes in the mantle, *Geol. Soc. Am. Bull., 86*, 1592-1600, 1975.

Anderson, D. L., Hotspots, polar wander, Mesozoic convection, and the geoid, *Nature, 297*, 391-393, 1982.

Anderson, O. L., Temperature profiles in the Earth, in R. J. O'Connell and W. S. Fyfe (eds.), **Evolution of the Earth**, Am. Geophys. Union, Washington, D. C., pp. 19-27, 1981.

Batiza, R. and D. Vanko, Petrology of young Pacific seamounts, *J. Geophys. Res., 89*, 11235-11260, 1984.

Betz, F. and H. H. Hess, The floor of the north Pacific ocean, *Geograph. Rev., 32*, 99-116, 1942.

Bonatti, E., C. G. A. Harrison, D. E. Fischer, J. Honnorez, J. G. Schilling, J. J. Stipp, and M. Zentelli, 1977, Easter volcanic chain (southeast Pacific): A mantle hot line, *J. Geophys. Res., 82*, 2457-2478, 1977.

Boss, A. B. and I. S. Sacks, Formation and growth of deep mantle plumes, *Geophys. J. Roy. Astron. Soc., 80*, 241-255, 1985.

Burke, K. and J. T. Wilson, 1976, Hot spots on the Earth's surface, *Sci. Am., 235*, 46-57, 1976.

Cathles, L. M., III, **The Viscosity of the Earth's Mantle**, Princeton Univ. Press, Princeton, N. J., 1975.

Chase, C. G., Subduction, the geoid, and lower mantle convection, *Nature, 282*, 464-468, 1979.

Chase, C. G. and M. K. McNutt, The geoid: effect of compensated topography and uncompensated oceanic trenches, *Geophys. Res. Lett., 9*, 29-32, 1982.

Chase, C. G. and D. R. Sprowl, The modern geoid and ancient plate boundaries, *Earth Planet. Sci. Lett., 62*, 314-320, 1983.

Chase, C. G. and D. R. Sprowl, Proper motion of hotspots: Pacific plate, *EOS, Trans. AGU, 65*, 1099 (abstract), 1984

Christenson, U., Convection with pressure and temperature dependent non-

Newtonian rheology, *Geophys. J. Roy. Astron. Soc., 77*, 343-384, 1984.

Clayton, R. W. and R. P. Comer, A tomographic analysis of mantle heterogeneities from body wave travel times, *EOS, Trans. AGU, 62*, 776 (abstract), 1983

Crough, S. T., Thermal origin of mid-plate hot-spot swells, *Geophys. J. Roy. Astron. Soc., 55*, 451-469, 1978.

Crough, S. T. and D. M Jurdy, Subducted lithosphere, hotspots, and the geoid, *Earth Planet. Sci. Lett., 48*, 15-22, 1980

Dalrymple, G. B. and D. A. Clague, Age of the Hawaiian-Emperor bend, *Earth Planet. Sci. Lett., 31*, 313-329, 1976.

Detrick, R. S. and S. T. Crough, Island subsidence, hot spots, and lithospheric thinning, *J. Geophys. Res., 83*, 1236-1244, 1978.

Dziewonski, A. M., Mapping the lower mantle: Determination of lateral heterogeneity in P velocity up to degree and order 6, *J. Geophys. Res., 89*, 5929-5952, 1984.

Eckhardt, D. H., Correlations between global features of terrestrial fields, *Math. Geol., 16*, 155-171, 1984.

Engebretson, D. C., A. Cox, and R. G. Gordon, Relative motions between oceanic plates of the Pacific basin, *J. Geophys. Res., 89*, 10291-10310, 1984.

Epp, D., Implications of volcano and swell heights for thinning of the lithosphere by hotspots, *J. Geophys. Res., 89*, 9991-9996, 1984a.

Epp, D., Possible perturbations to hotspot traces and implications for the origin and structure of the Line islands, *J. Geophys. Res., 89*, 11273-11286, 1984b.

Gubbins, D., T. G. Masters, and J. A. Jacobs, Thermal evolution of the Earth's core, *Geophys. J. Roy. Astron. Soc., 59*, 57-99, 1979.

Hadley, D. M., G. S. Stewart, and J. E. Ebel, Yellowstone: Seismic evidence for a chemical plume, *Science, 93*, 1237-1239, 1976.

Hager, B. H., Global isostatic geoid anomalies for plate and boundary layer models of the lithosphere, *Earth Planet. Sci. Lett., 63*, 97-109, 1983.

Hager, B. H., Subducted slabs and the geoid: Constraints on mantle rheology and flow, *J. Geophys. Res., 89*, 6003-6015, 1984.

Hager, B. H., R. W. Clayton, M. A. Richards, R. P. Comer, and A. M. Dziewonski, Lower mantle heterogeneity, dynamic topography, and the geoid, *Nature,*

313, 541-545, 1985.

Hager, B. H. and R. J. O'Connell, Kinemetic models of large-scale mantle flow, *J. Geophys. Res., 84*, 1031-1048, 1979.

Hager, B. H. and R. J. O'Connell, A simple global model of plate dynamics and mantle convection, *J. Geophys. Res., 86*, 4843-4867, 1981.

Hager, B. H. and M. A. Richards, The generation of long-wavelength geoid anomalies: Implications for mantle structure, *Terra Cognita, 4*, 247-248, 1984.

Hong, H. J. and D. A. Yuen, Dynamical consequences on surface deformations and geoids from equation of state, *EOS, Trans. AGU, 66*, 1075 (abstract), 1985.

Iyer, H. M., Anomalous delays of teleseismic P waves in Yellowstone National Park, *Nature, 253*, 425-428, 1975.

Jarrard, R. D. and D. A. Clague, Implications of Pacific island and seamount ages for the origin of volcanic chains, *Rev. Geophys. Space Phys., 15*, 57-76, 1977.

Kaula, W. M., Tesseral harmonics of the gravitational field and geodetic datum shifts derived from camera observations of satellites, *J. Geophys. Res., 68*, 473-484, 1963.

Kaula, W. M., Earth's gravity field: Relation to global tectonics, *Science, 167*, 977-985, 1970.

Kiefer, W. S., M. A. Richards, B. H. Hager, and B. G. Bills, A dynamic model of Venus' gravity field, *Geophys. Res. Lett.*, in press.

Lerch, F. J., S. M. Klosko, and G. B. Patch, A refined gravity model from LAGEOS (GEM-L2), *NASA Tech. Memo. 84986*, 1983.

Loper, D. E., A simple model of whole-mantle convection, *J. Geophys. Res., 90*, 1809-1836, 1985.

Loper, D. E. and F. D. Stacey, The dynamical and thermal structure of deep mantle plumes, *Phys. Earth Planet. Int., 33*, 304-317, 1983.

Masters, G. T. H. Jordan, P. G. Silver, and F. Gilbert, Aspherical Earth structure from fundamental spheroidal-mode data, *Nature, 298*, 609-613, 1982.

McKenzie, D. P., Surface deformation, gravity anomalies and convection, *Geophys. J. Roy. Astron. Soc., 48*, 211-238, 1977.

McKenzie, D. P. and C. Bowin, The relationship between bathymetry and gravity in the Atlantic ocean, *J. Geophys. Res., 81*, 1903-1915, 1976.

McNutt, M. K., Lithospheric flexure and thermal anomalies, *J. Geophys. Res., 89*, 11180-11194, 1984.

Morgan, W. J., Gravity anomalies and convection currents. I. A sphere and cylinder sinking beneath the surface of a viscous fluid, *J. Geophys. Res., 70*, 6175-6187, 1965.

Morgan, W. J., Plate motions and deep mantle convection, *Geol. Soc. Am. Mem., 132*, 7-22, 1972.

Morgan, W. J., Hot spot tracks and the opening of the Atlantic and Indian oceans, in **The Sea**, *7*, C. Emiliani (ed.), Wiley Interscience, NY, pp. 443-487, 1981.

Nakiboglu, S. M., Hydrostatic theory of the Earth and its mechanical implications, *Phys. Earth Planet. Int., 28*, 302-311, 1982.

Nataf, H.-C., I. Nakanishi, and D. L. Anderson, Anisotropy and shear-velocity heterogeneities in the upper mantle, *Geophys. Res. Lett., 11*, 1109-1112, 1984.

Nataf, H.-C., I. Nakanishi, and D. L. Anderson, Measurements of mantle wave velocities and inversion for lateral heterogeneities and anisotropy. Part III: Inversion, *J. Geophys. Res.*, in press, 1986.

O'Connell, R. J., Pleistocene glaciation and the viscosity of the lower mantle, *Geophys. J. Roy. Astron. Soc., 23*, 299-327, 1971.

O'Connell, R. J. and B. H. Hager, On the thermal state of the Earth, in **Physics of the Earth's Interior**, A. Dziewonski and E. Boschi (eds.), North-Holland, Amsterdam, pp. 270-317, 1980.

Olson, P. and H. Singer, Creeping plumes, *J. Fluid Mech., 158*, 511-531, 1985.

Parmentier, E. M., D. L. Turcotte, and K. E. Torrance, Numerical experiments on the structure of mantle plumes, *J. Geophys. Res., 80*, 4417-4424, 1975.

Parsons, B. and S. Daly, The relationship between surface topography, gravity anomalies and the temperature structure of convection, *J. Geophys. Res., 88*, 1129-1144, 1983.

Pekeris, C. L., Thermal convection in the interior of the Earth, *Mon. Not. Roy. Astron. Soc., Geophys. Suppl., 3*, 343-367 1935.

Peltier, W. R., Ice age geodynamics, *Ann. Rev. Earth Planet. Sci., 9*, 199-225, 1981.

Pilger, R. H., The origin of hotspot traces: Evidence from eastern Australia, *J. Geophys. Res., 87*, 1825-1834, 1982.

Ricard, Y., L. Fleitout, and C. Froidevaux, Geoid heights and lithospheric stresses for a dynamical Earth, *Annales Geophysicae, 2*, 267-286, 1984.

Richards, M. A. and B. H. Hager, Geoid anomalies in a dynamic Earth, *J. Geophys. Res., 89*, 5487-6002, 1984.

Richards, M. A. and B. H. Hager, The Earth's geoid and the large-scale structure of mantle convection, **Proc. NATO Adv. Study Inst.**, S. K. Runcorn (editor), in press, 1986.

Richter, F. M. and D. P. McKenzie, On some consequences and possible causes of layered convection, *J. Geophys. Res., 86*, 6133-6142, 1981.

Runcorn, S. K., Satellite gravity measurements and a laminar viscous flow model of the Earth's mantle, *J. Geophys. Res., 69*, 4389-4394, 1964.

Schlanger, S. O., M. O. Garcia, B. H. Keating, J. J. Naughton, W. W. Sager, J. A. Haggerty, J. A. Philpotts, and R. A. Duncan, Geology and geochronology of the Line islands, *J. Geophys. Res., 89*, 11261-11272, 1984.

Schroeder, W., The empirical age-depth relation and depth anomalies in the Pacific ocean basin, *J. Geophys. Res., 89* 9873-9883, 1984.

Sleep, N. H., Segregation of magma from a mostly crystalline mush, *Geol. Soc. Am. Bull., 85*, 1225-1232, 1974.

Sleep, N. H., The double seismic zone in downgoing slabs and the viscosity of the mesosphere, *J. Geophys. Res., 84*, 4565-4571, 1979.

Sleep, N. H., Tapping of magmas from ubiquitous mantle heterogeneities: An alternative to mantle plumes? *J. Geophys. Res., 89*, 10029-10041 1984a.

Sleep, N. H., Lithospheric delamination beneath Hawaii: No plume, *EOS, Trans. AGU, 65*, 1087 (abstract), 1984b.

Sleep, N. H. and R. J. Phillips, Gravity and lithospheric stress on the terrestrial planets with reference to the Tharsis region of Mars, *J. Geophys. Res., 90*, 4469-4489, 1985.

Solomon, S. C. and N. H. Sleep, Some models for absolute plate motions, *J. Geophys. Res., 79*, 2537-2567, 1974.

Sneddon, I. N., **Fourier Transforms**, McGraw-Hill, New York, 1951.

Stacey, F. D. and D. E. Loper, The thermal boundary-layer interpretation of D$''$ and its role as a plume source, *Phys. Earth Planet. Int., 33*, 45-55, 1983.

Stefanic, M. and D. M. Jurdy, 1984, The distribution of hot spots, *J. Geophys.*

Res., 89, 9919-9925, 1984.

Tanimoto, T., The Gilbert-Backus approach to the three-dimensional structure in the upper mantle. II. SH and SV velocity, *Geophys. J. Roy. Astron. Soc.*, in press, 1986.

Turcotte, D. L. and E. R. Oxburgh, Mid-plate tectonics, *Nature, 244*, 337-339, 1973.

Turcotte, D. L. and E. R. Oxburgh, Stress accumulation in the lithosphere, *Tectonophysics, 35*, 183-199, 1976.

Verhoogen, J. 1973, Thermal regime of the Earth's core, *Phys. Earth Planet. Int., 7*, 47-58, 1973.

Von Herzen, R. P., R. S. Detrick, S. T. Crough, D. Epp, and V. Fehn, Thermal origin of the Hawaiian swell: Heat flow evidence and thermal models, *J. Geophys. Res., 87*, 6711-6723, 1982.

Watts, A. B., An analysis of isostasy in the world's oceans. I. Hawaiian-Emperor seamount chain, *J. Geophys. Res., 83*, 5989-6004, 1978.

Wilson, J. T., A possible origin of the Hawaiian Islands, *Can. J. Phys., 41*, 863-870, 1963.

Woodhouse, J. H. and A. M. Dziewonski, Mapping the upper mantle: three dimensional modelling of Earth structure by inversion of seismic waveforms, *J. Geophys. Res., 89*, 5953-5986, 1984.

Yuen, D. A. and W. R. Peltier, Mantle plumes and the thermal stability of the D$''$ layer, *Geophys. Res. Lett., 9*, 625-628, 1980.

Yuen, D. R., Sabadini, R., and E. V. Boschi, Viscosity of the lower mantle as inferred from rotational data, *J. Geophys. Res., 87*, 10745-10762, 1982.

Yuen, D. A. and G. Schubert, Mantle plumes: A boundary layer approach for Newtonian and non-Newtonian temperature-dependent rheologies, *J. Geophys. Res., 81*, 2499-2510, 1976.

Table Captions

Table 1 - Hotspot locations used to obtain the spherical harmonic expansion of the hotspot distribution.

Table 2 - Correlation coefficients at harmonic degree 6 between upper mantle shear velocity models (Tanimoto, 1986; Woodhouse and Dziewonski, 1984) and the observed geoid, the slab residual geoid, and the hotspot distribution.

TABLE I: Hotspot Locations

Lat.	Long.	Name
50	7	Eifel, Belgium
23	6	Hoggar Mountains, Algeria
21	17	Tibesti, Chad
13	24	Jebel Marra, Sudan / Darfur
4	9	Mt. Cameroon
-3	36	Lake Victoria / East Africa
12	42	Afar / Ethiopia
-12	44	Comores Islands
-21	56	Reunion
-45	45	Crozet
-45	65	Kerguelen
-35	80	Christmas Island, Indian Ocean / Amsterdam
-40	150	Tasmania
45	-111	Yellowstone
37	-104	Raton, New Mexico
27	-113	Baja California / Guadalupe Seamount
53	-135	Bowie Seamount / Kodiak Seamounts
46	-128	Juan de Fuca / Cobb Seamount
20	-155	Hawaii
-29	-140	MacDonald Seamount / Cook--Austral Islands
-18	-148	Mehetia / Society Islands / Tahiti
-27	-129	Pitcairn Island / Gambier Islands
3	167	Caroline Islands
-11	-139	Marquesas Islands
-27	-109	Easter Island
0	-91	Galapagos Islands
-27	-80	San Felix, Nazca Plate
-34	-79	Juan Fernandez, Nazca Plate
72	-8	Jan Mayen
64	-20	Iceland
30	-60	Bermuda
38	-28	Azores
33	-17	Madeira
28	-17	Canary Islands
29	-29	New England Seamounts / Great Meteor Seamount
15	-24	Cape Verde
-4	-32	Fernando
-17	-25	Arnold Seamount
-21	-29	Trindade
-8	-14	Ascension
-16	-6	St. Helena
-37	-12	Tristan de Cunha
-42	0	Discovery Seamount
-54	4	Bouvet
-32	16	Vema Seamount
-78	167	Mt. Erebus
-15	-168	Samoa

TABLE II: Degree 6 Correlations (significance)

	Upper Mantle Velocity Model		
	TSV(350km)	TSV(250km)	W&D(200-500km)
geoid	-.63(>98%)	-.67(>99%)	-.58(>95%)
residual geoid	-.72(>99%)	-.74(>99%)	-.65(>99%)
hotspots	-.54(>95%)	-.49(>90%)	-.70(>99%)

Figure Captions

Figure 1 - (a),(b) Observed long-wavelength geoid (Lerch et al., 1983) referred to the hydrostatic figure of the Earth (Nakiboglu, 1982). In (b) the degree 2-3 components have been removed. Hotspot locations are indicated by black dots. Continents and plate boundaries are also shown. Geoid lows are shaded; cylindrical equidistant projection.

(c),(d) Residual geoid after the subducted slab geoid model of Hager (1984) is removed.

Figure 2 - Log-log comparison of root mean square harmonic coefficient amplitudes as a function of spherical harmonic degree. Units are as follows: Observed and residual geopotentials, $\gamma M/R$ (fraction of geopotential at surface), (γ is the gravitational constant, M the mass of the Earth, and R the Earth's radius.) Hotspot distribution, $4.1x\,10^6$ hotspots per Earth area; Lower mantle P-velocity (Clayton and Comer, 1983), 10^4 km/sec. Geopotentials may be converted to geoid elevations by dividing by the gravitational acceleration at the surface.

Figure 3 - Degree-by-degree correlations, r_l, between the hotspot distribution and the slab residual geoid (solid line). Correlations between the slab geoid model (Hager, 1984) and the observed geoid are shown for comparison (dashed line). Contours give the confidence of correlation, with a confidence level of 0.98

indicating only a 2% chance that the correlation is random.

Figure 4 - Degree 2 comparison of the slab residual geoid, the vertically averaged lower mantle P-wave velocity model (Clayton and Comer, 1983), and the hotspot density distribution. Geoid lows, slow velocity anomalies, and low hotspot density areas are shaded. Hotspot density contour intervals are in units of 16.5 hotspots per Earth area.

Figure 5 - Degree 6 comparison of the slab residual geoid, upper mantle shear velocity (200-500 km: Woodhouse and Dziewonski, 1984), and the hotspot density distribution. Geoid lows, fast velocity anomalies, and low hotspot density areas are shaded. Hotspot density contour intervals are in units of 33 hotspots per Earth area.

Figure 6 - Best-fitting hotspot/geoid response curve (solid dots) according to equation 3 of text. Error bars (2σ) indicate the uncertainty of the fit. Open circles give the best-fitting curve under the assumption of equal noise in both the slab residual geoid and the hotspot distribution (error bars not shown).

Figure 7 - Slab residual geoid in harmonic degree bands 4-6, 7-12, and 10-20. Hotspot locations are shown by black dots.

Figure 8 - Dynamic response functions, $G_l(r)$, for surface density contrasts of spherical harmonic degrees 2, 4, 6, and 8 plotted against radius, r, for six

Earth models. Models U, for uniform composition, left, permit mantle-wide flow; models C, right, have a (chemical) barrier at 670 km depth, causing stratification into separate upper and lower mantle flow systems. Models U1 and C1 have uniform viscosity; models U10 and C10 have a factor of 10 viscosity increase below 670 km; models U100 and C100 have a factor of 100 increase. The geoid responses are normalized to the geoid which would be obtained if the harmonic density contrasts were placed at the top surface with no dynamic compensation allowed.

Figure 9 - Residual depth anomaly map of the Hawaiian swell (adapted from Schroeder, 1984). Flow stagnation contours for 300^0K and 1000^0K kinematic plume models are shown by bold lines. Cross sections AA' and BB' are plotted in Figure 20.

Figure 10 - Example finite element grid used in plume and slab models.

Figure 11 - Illustration of the A, B, and C plume models. Horizontal and vertical scales are equal. η_0 is the reference viscosity.

Figure 12 - Pseudo geoid response functions (see text) for the first three harmonics (wavelengths corresponding to degrees 4,8,12) of the cylinder (or box) for the finite element model A plume (solid line) and the high viscosity slab (dashed line). The dotted line gives the analytical solution for uniform mantle viscosity.

Figure 13 - Excess geoid signal perturbation relative to the isoviscous case, for the range of excess plume temperatures and viscosity exponents, β, tested at plume radius r_0=70 km. The l=4, 8, and 12 curves are for the first three harmonics of the cylinder for halo model A.

Figure 14 - Buoyancy flux (r_0=70 km) as a function of excess plume temperature and β for halo model A. The background viscosity is 10^{21} Pa-sec

Figure 15 - Buoyancy flux as a function of plume radius for halo model A. The right-hand vertical scale is linear and gives the fourth root of the flux. Solid lines are for excess temperatures of 400^0K and 800^0K with β=28. Dashed lines are for the isoviscous models (β=0).

Figure 16 - Geoid signal perturbation (excess), relative to the isoviscous geoid, as a function of radius and viscosity contrast. The l=4, 8, and 12 curves are for the first three harmonics of the cylinder for the pipe model.

Figure 17 - Buoyancy flux as a function of radius and viscosity contrast for the pipe model. The flux is normalized to the square of the excess temperature for density ρ_0=5.14 and volume coefficient of thermal expansion $3x\,10^5/^0$K. The right-hand scale is linear and gives the fourth root of the flux. Dashed lines give the theoretical flux for an infinite rigid pipe (mantle) for the same interior pipe viscosities and buoyancy forces (see text).

Figure 18 - Comparison of global hotspot response curve (solid line with error bars) and several dynamic models. Solid triangles give the l=4,8,12 geoid signal for plume model B (β=35). Solid diamonds are for model C (β=35). Model C′ (β=0), indicated by open diamonds, has no viscosity contrast between the mantle and the plume. The "spherical Earth" model (dashed lines) was calculated analytically using the method of Richards and Hager (1984) with a 200 km radius plume, average temperature contrast 300^0K, and no viscosity contrast. The dotted line gives the (spherical) analytical calculation for the geoid spectrum from lithospheric delamination.

Figure 19 - Pseudo geoid response functions (see text) for the model C plume (solid line), subducted slab (dashed line), and slab with weakened lithosphere (dash-dot line). The dotted line gives the analytical solution for the purely layered response.

Figure 20 - Comparison of dynamic topography from Models B and C with the observed Hawaiian swell topography. The heavy dotted line is from section A-A′ of Figure 9, and the lighter dotted line is from section B-B′ 500 km WNW of Hawaii ("anomalous" bathymetry adapted from Schroeder, 1984). Light and heavy solid curves are for strongly temperature dependent viscosity (β=35) in models B and C, respectively. Light and heavy dashed curves are for no viscosity contrast between plume and mantle (β=0) in models B and C, respectively. Deformation profiles for the theoretical models decay toward the zero level out to 5000 km from the plume axis, but are truncated in this figure

in order to emphasize deformation near the swell itself.

Figure B1 - Illustration of the geometry for the high viscosity slab calculations. Horizontal and vertical scales are equal.

Figure B2 - Pseudo response curves (l=5,10) for models L100.u (dotted line), L100.slab (solid line), L100.slab200 (long dashes), and L100.slab400 (short dashes).

Figure B3 - Pseudo response curves (l=5,10) for models LU100.u (dotted line), LU100.slab (solid line), LU100.slab200 (long dashes), and LU100.slab400 (short dashes).

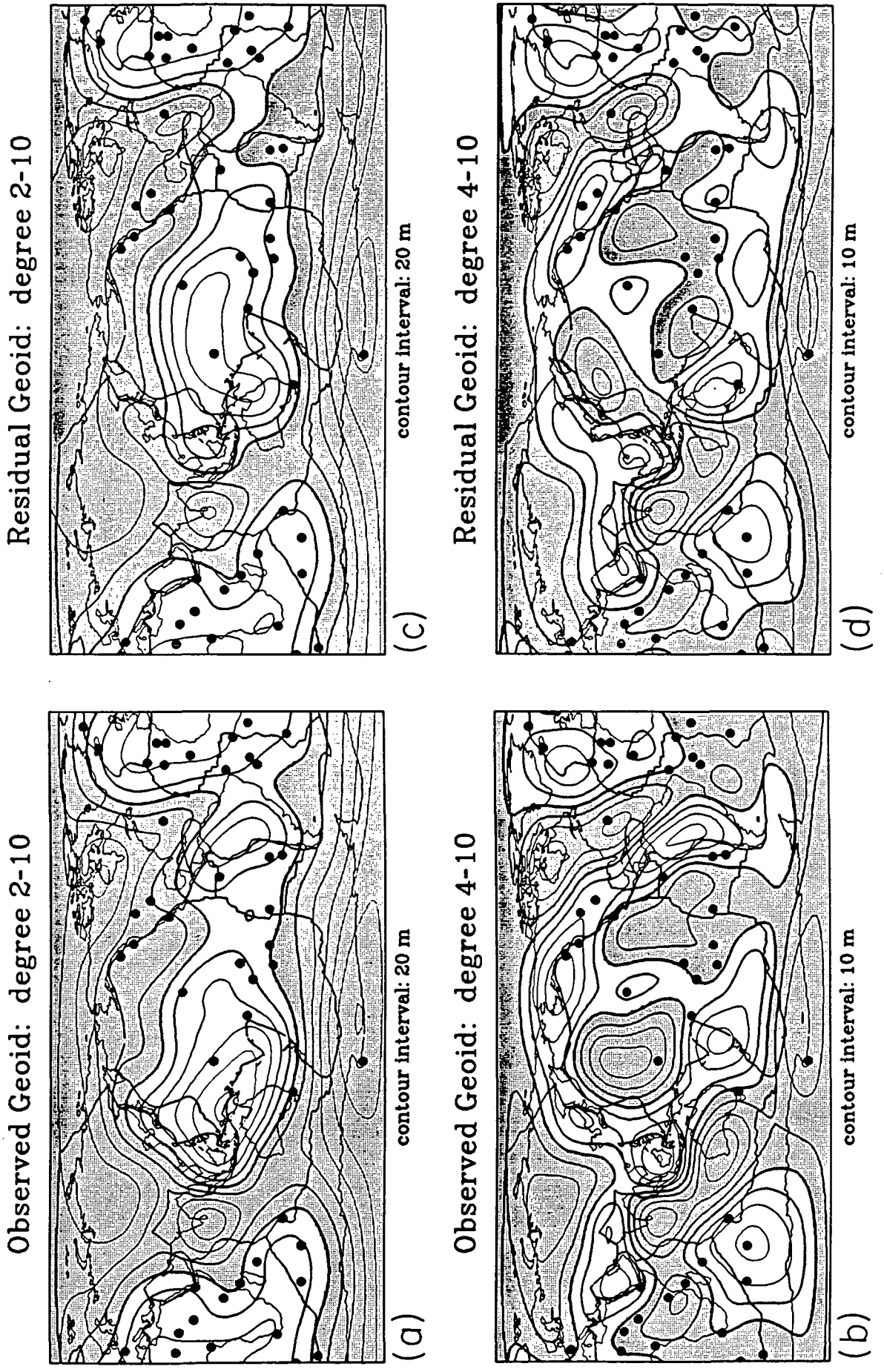
Observed Geoid: degree 2-10
contour interval: 20 m
(a)
Residual Geoid: degree 2-10
contour interval: 20 m
(c)
Observed Geoid: degree 4-10
contour interval: 10 m
(b)
Residual Geoid: degree 4-10
contour interval: 10 m
(d)

Figure 1

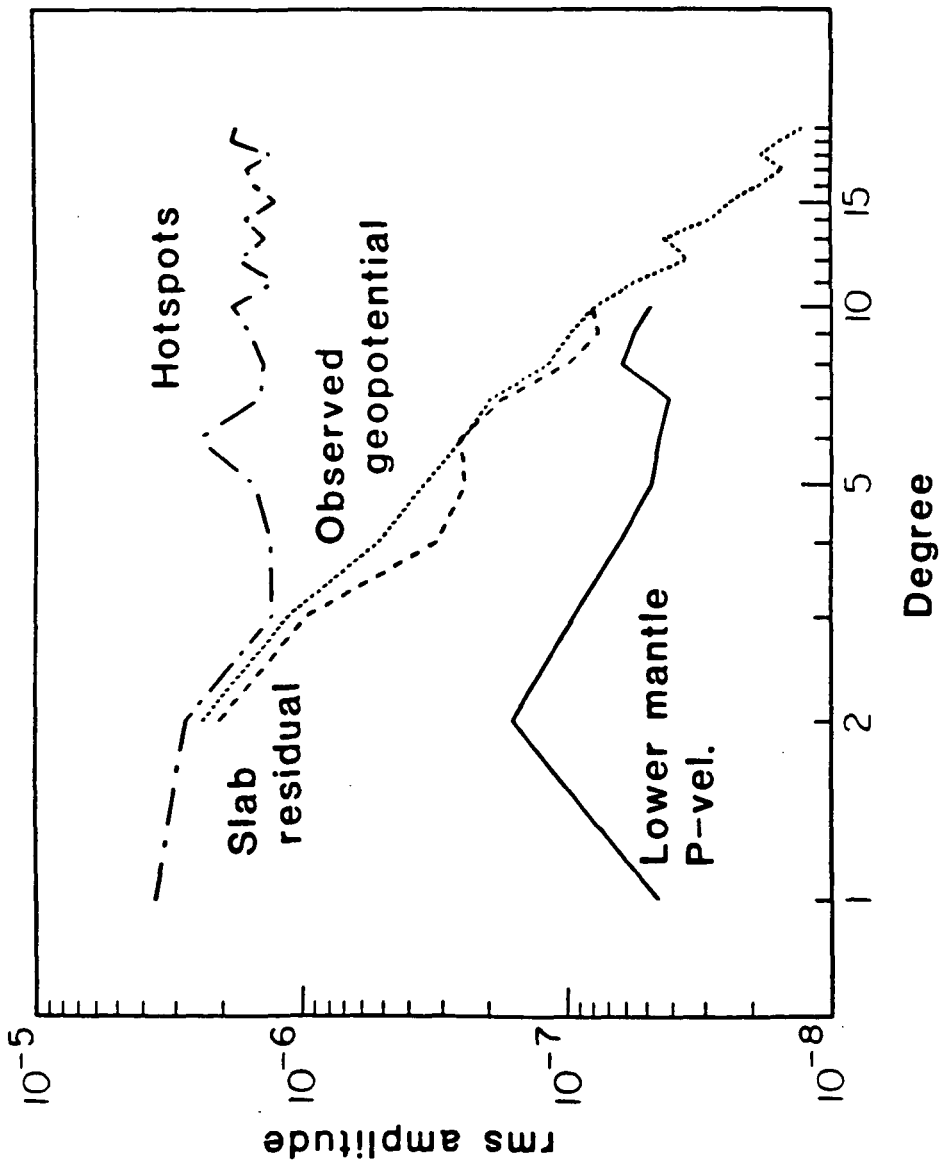
Hotspots
Observed geopotential
Slab residual
Lower mantle P-vel.
rms amplitude
10^{-5}
10^{-6}
10^{-7}
10^{-8}
1
2
5
10
15
Degree

Figure 2

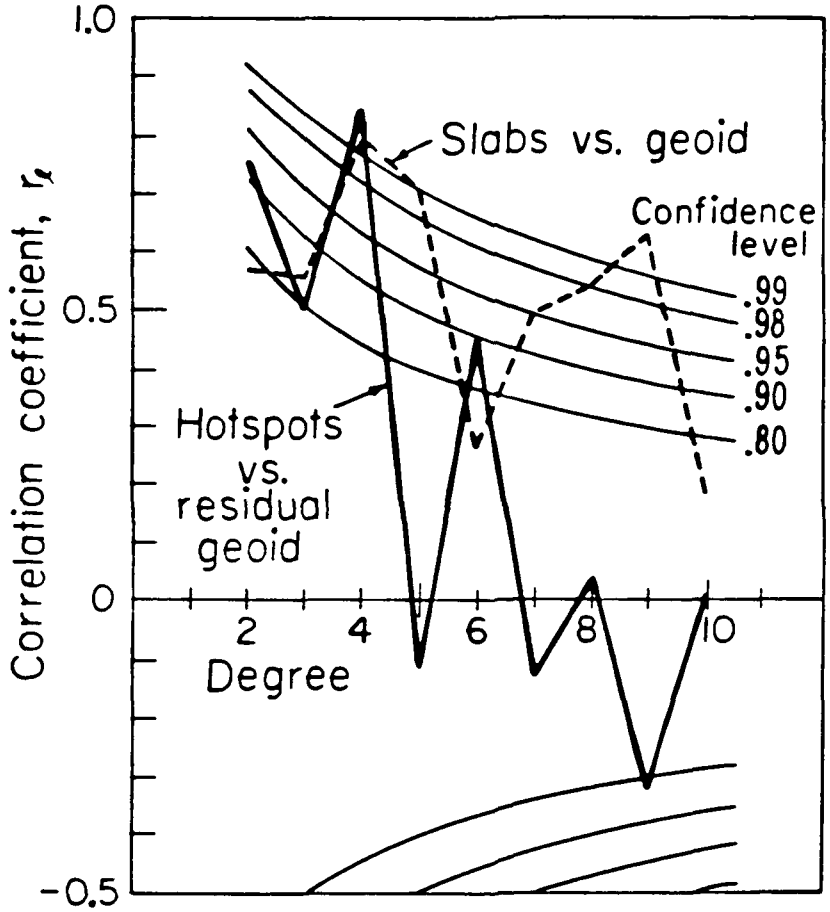
1.0
0.5
0
-0.5
Correlation coefficient, r_x
Slabs vs. geoid
Confidence level
.99
.98
.95
.90
.80
Hotspots vs. residual geoid
2
4
6
8
10
Degree

Figure 3

Residual Geoid: degree 2

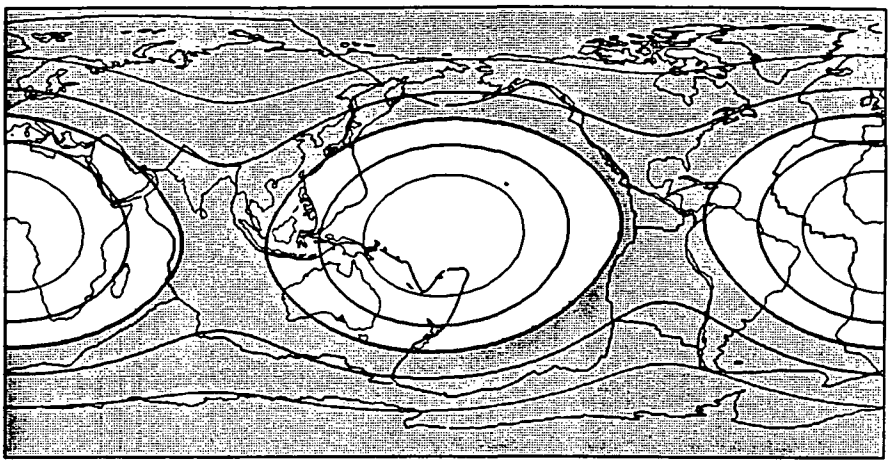

(a) contour interval: 20 m

Lower Mantle P-Wave Velocity: degree 2

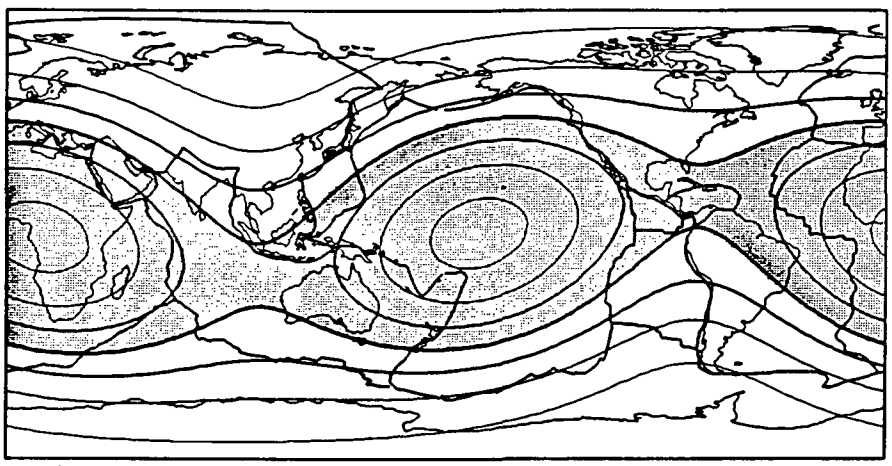

(b) contour interval: 2 m/sec

Hotspot Density: degree 2

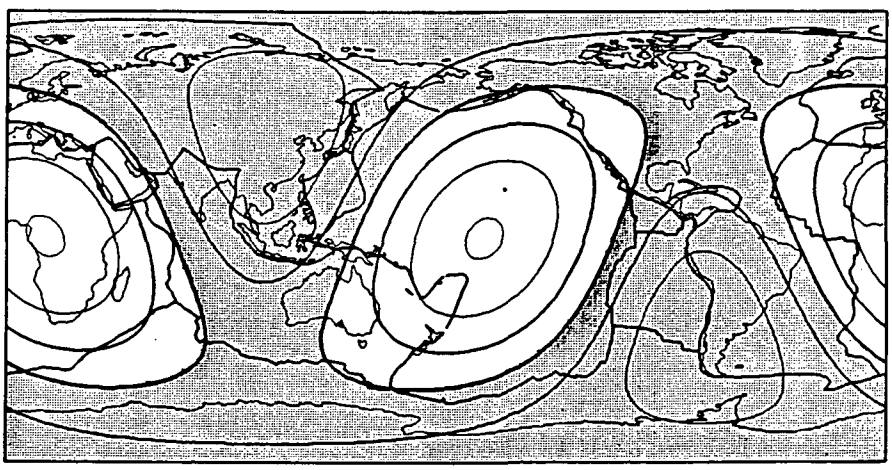

(c)

Figure 4

Residual Geoid: degree 6

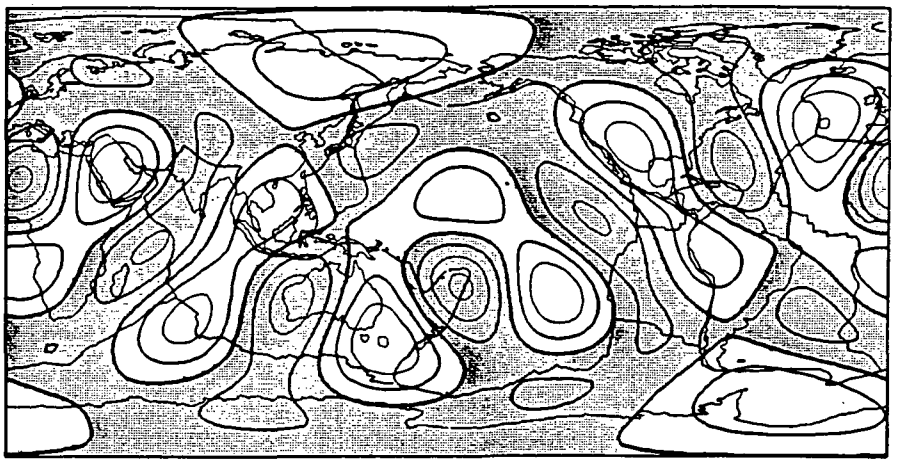

(a) contour interval: 5 m

Upper Mantle Shear Velocity: degree 6

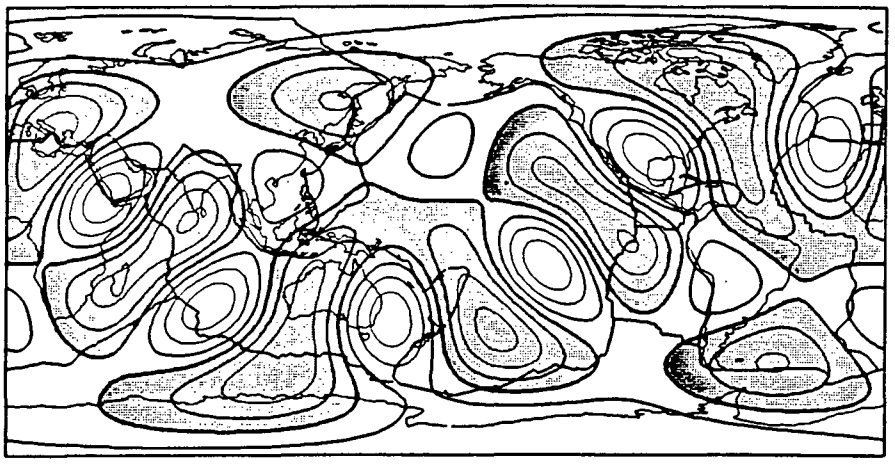

(b) contour interval: 10 m/sec

Hotspot Density: degree 6

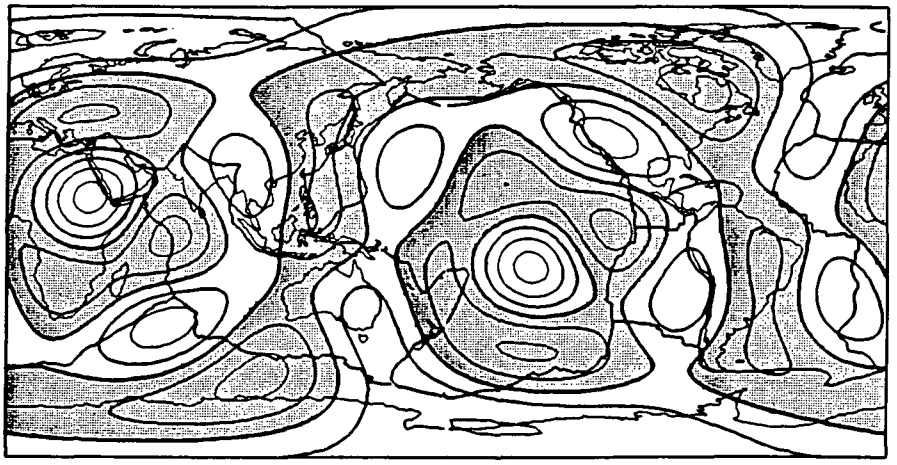

(c)

Figure 5

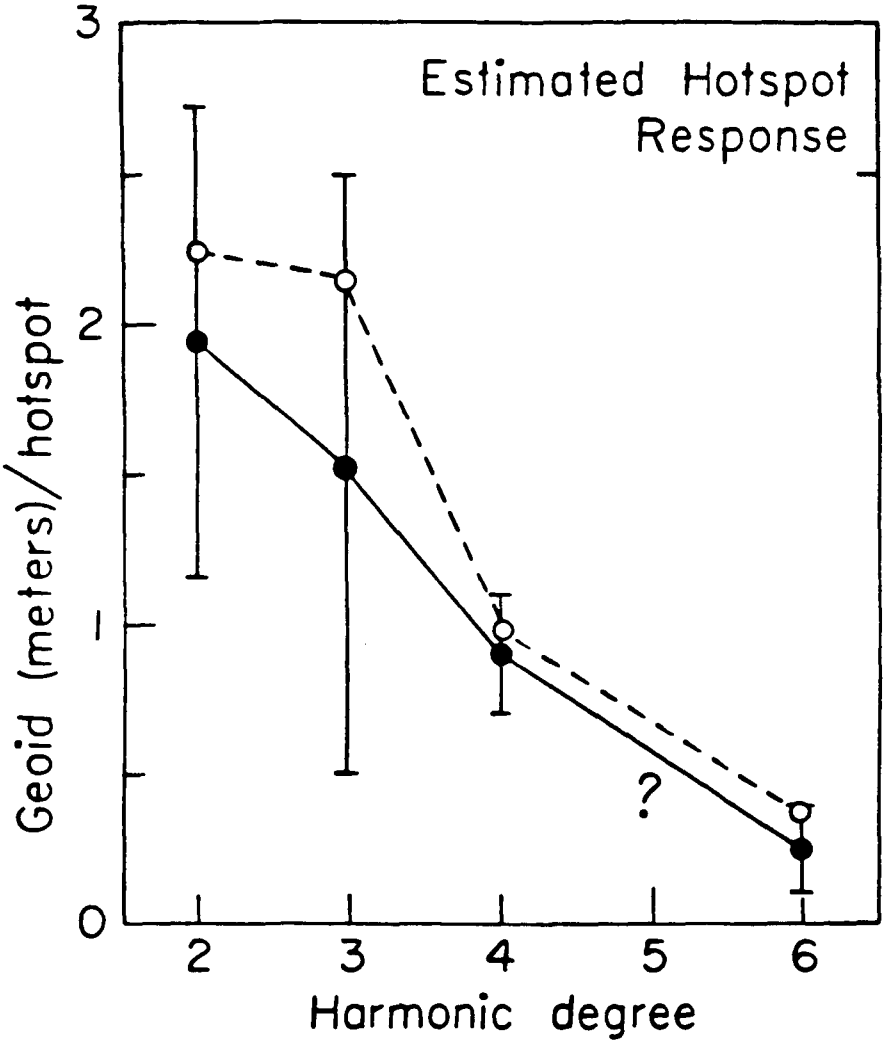
Estimated Hotspot
Response
Geoid (meters)/hotspot
3
2
1
0
2
3
4
5
6
?
Harmonic degree

Figure 6

Residual Geoid: degree 4-6

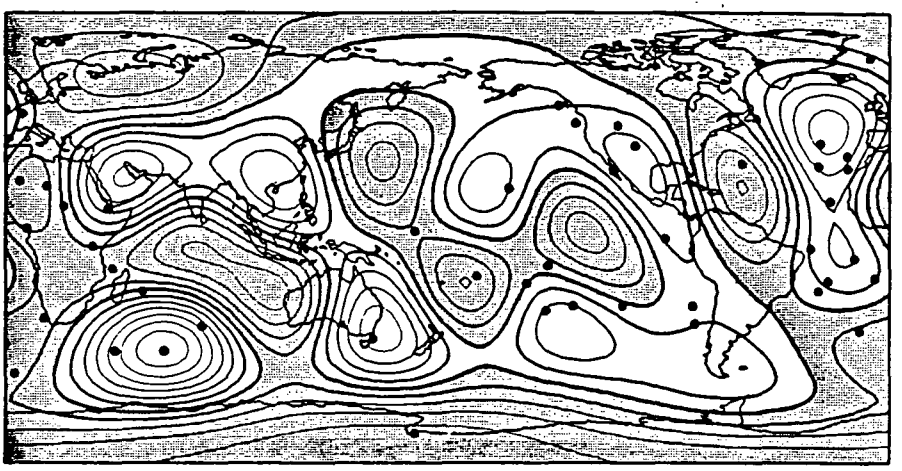

contour interval: 5 m (a)

Residual Geoid: degree 7-12

contour interval: 5 m (b)

Residual Geoid: degree 10-20

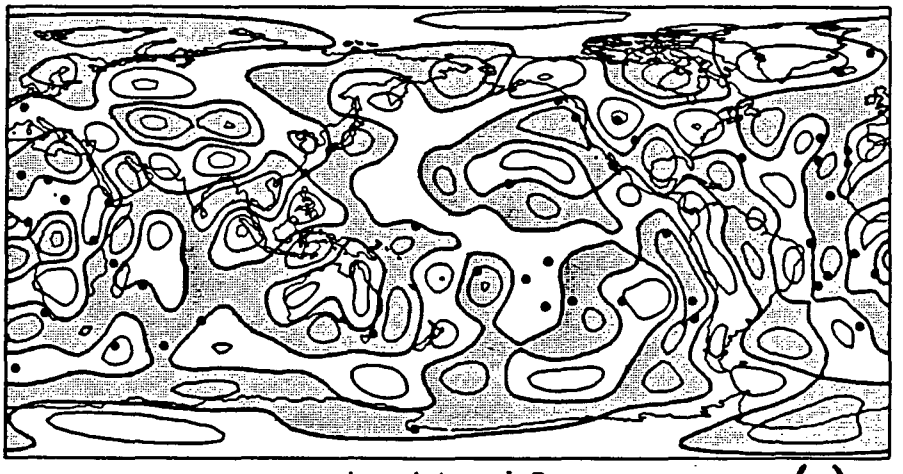

contour interval: 5 m (c)

Figure 7

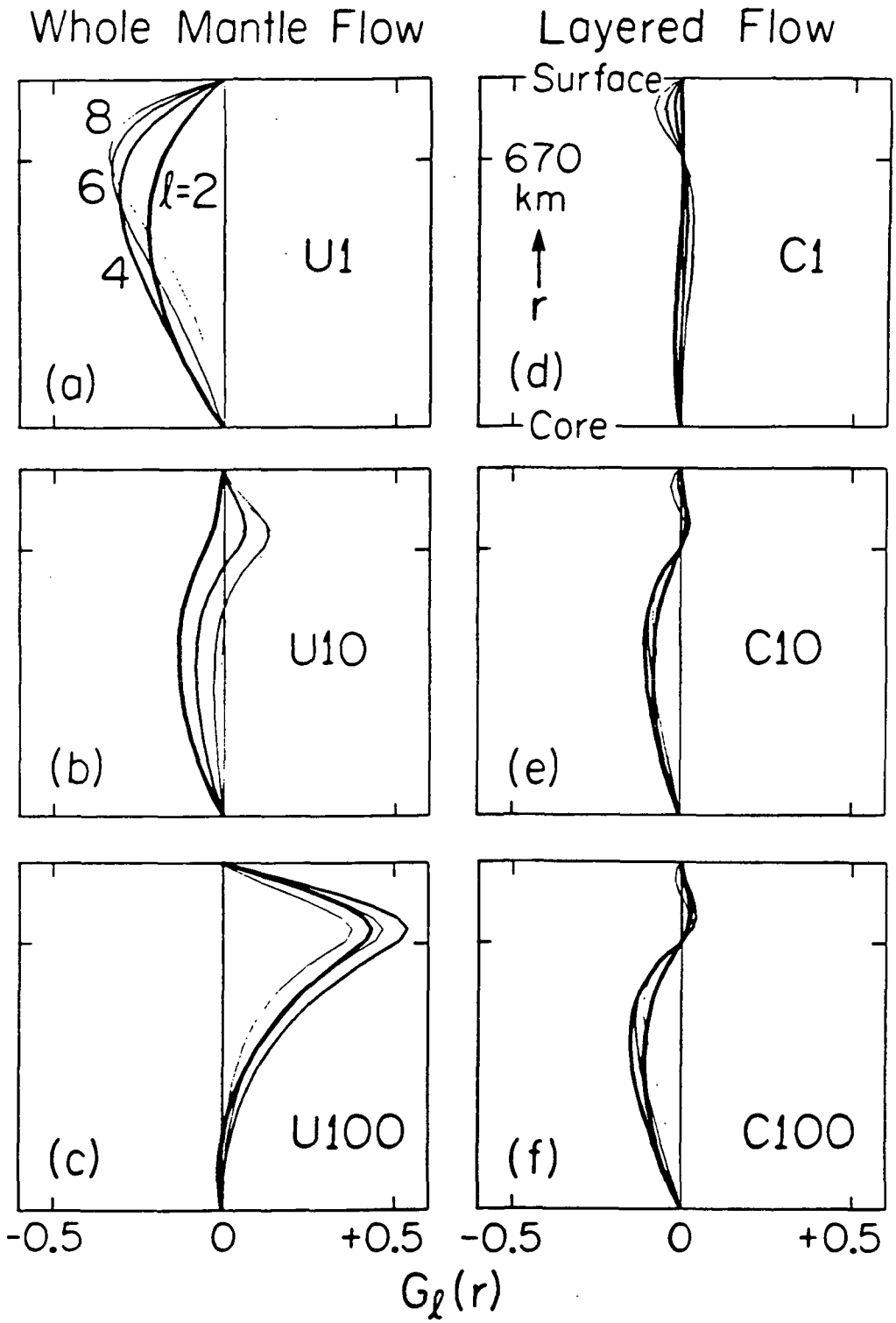
Whole Mantle Flow
Layered Flow
Surface
670
km
r
Core
8
6
4
ℓ=2
U1
C1
(a)
(d)
U10
C10
(b)
(e)
U100
C100
(c)
(f)
-0.5
0
+0.5
-0.5
0
+0.5
$G_\ell(r)$

Figure 8

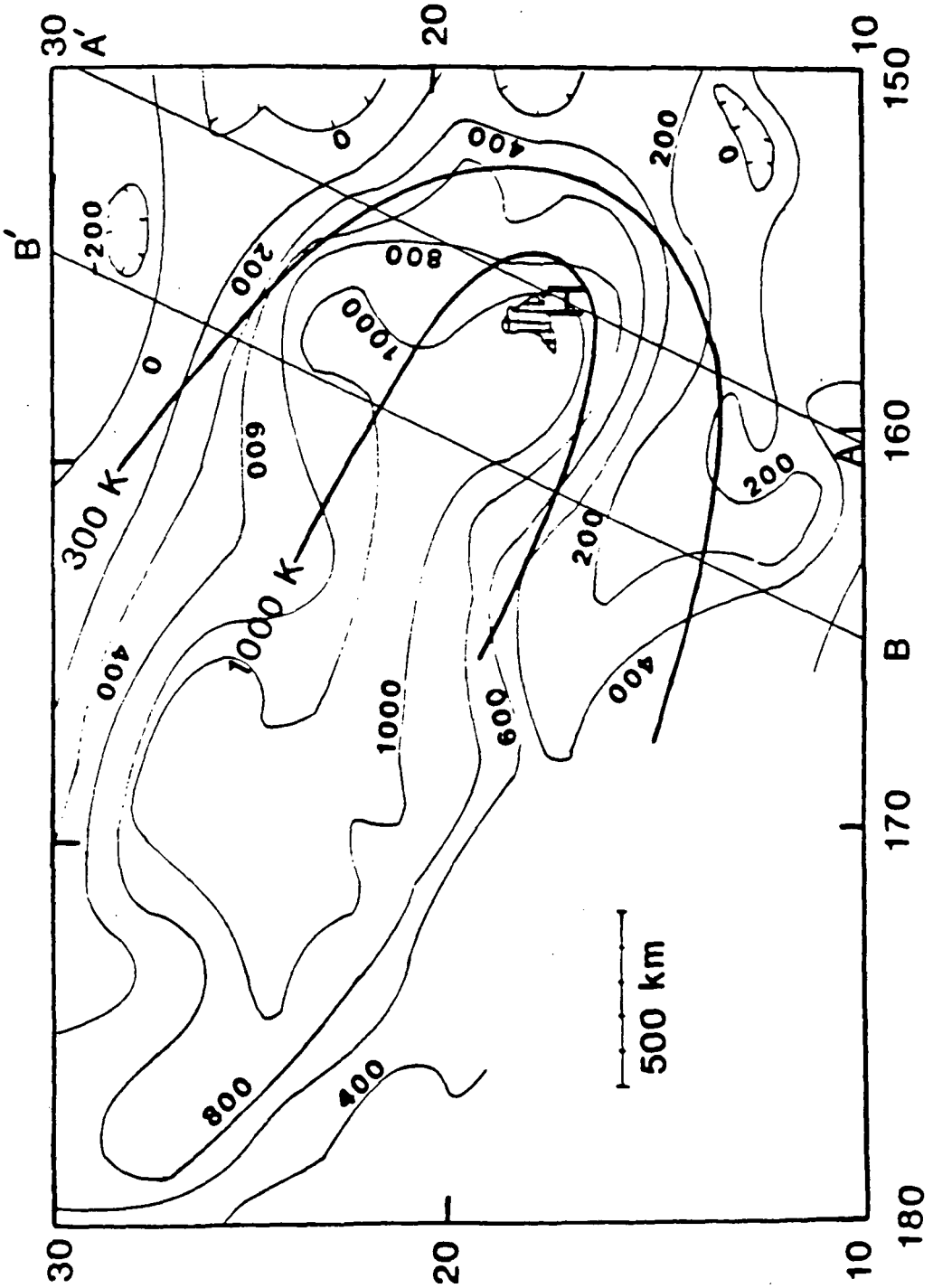
30
A'
20
10
150
B'
200
0
400
200
800
200
1000
0
600
300 K
1000 K
400
1000
600
400
200
200
200
A
160
B
170
500 km
800
400
30
20
10
180

Figure 9

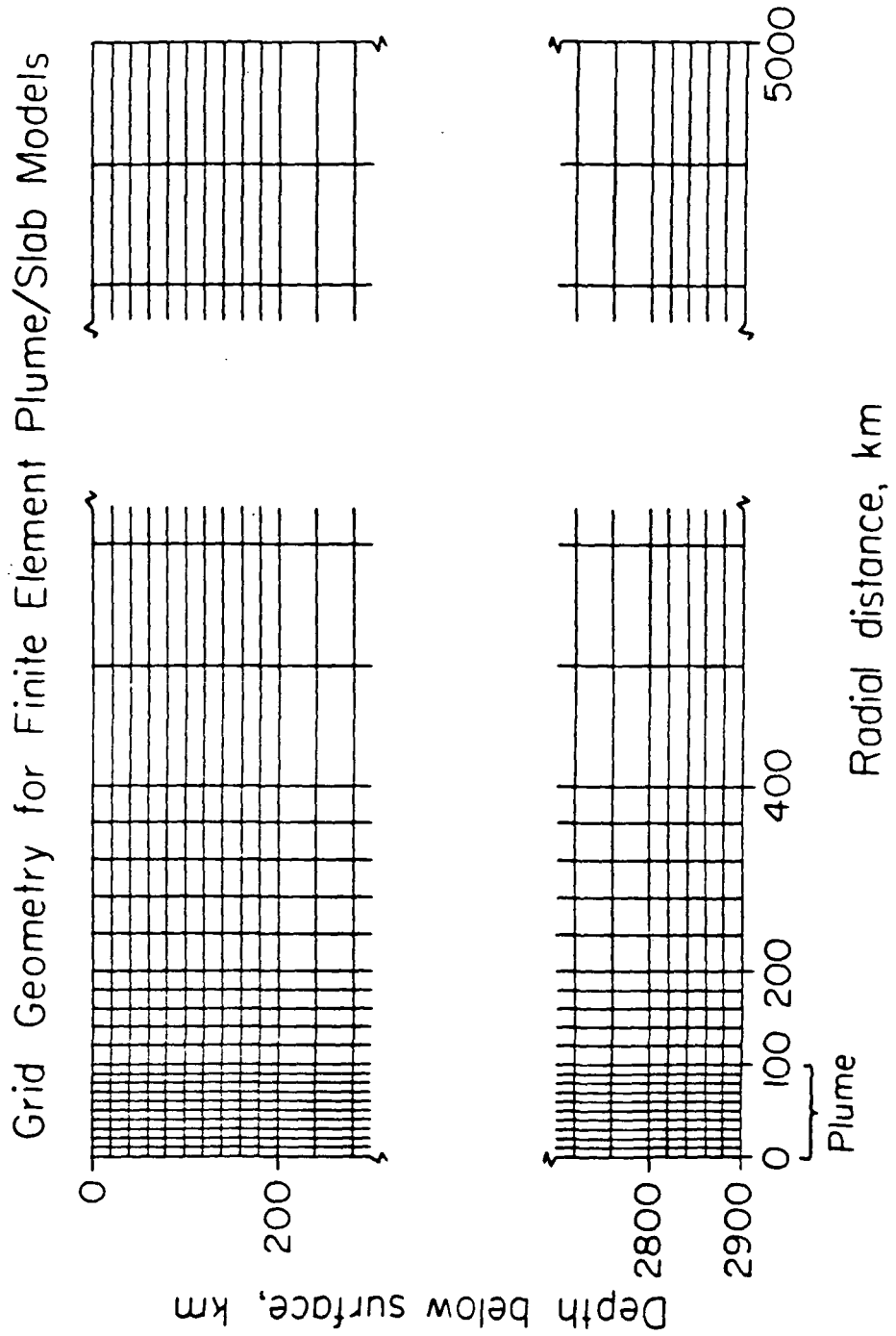
Grid Geometry for Finite Element Plume/Slab Models
Depth below surface, km
0
200
2800
2900
0
100
200
400
5000
Plume
Radial distance, km

Figure 10

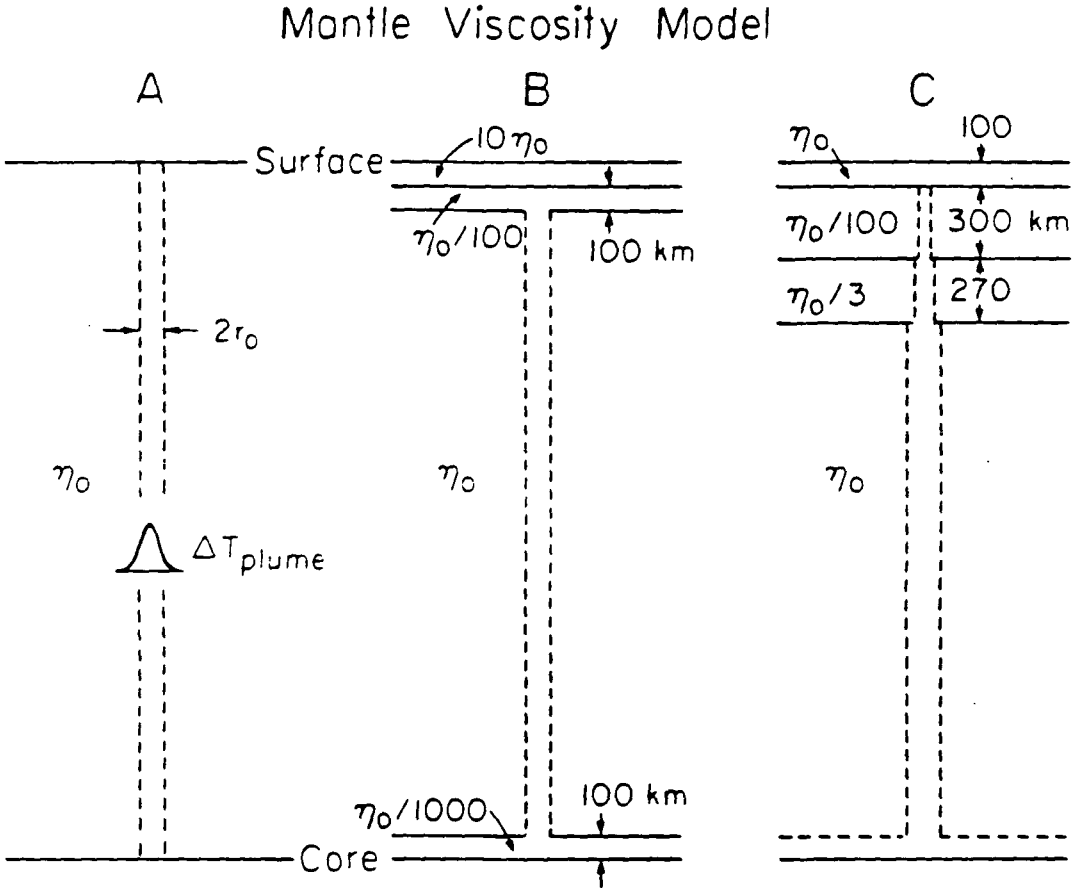
Mantle Viscosity Model
A
B
C
Surface
$10\eta_o$
η_o
100
$\eta_o/100$
100 km
$\eta_o/100$
300 km
$\eta_o/3$
270
$2r_o$
η_o
η_o
η_o
ΔT_{plume}
$\eta_o/1000$
100 km
Core

Figure 11

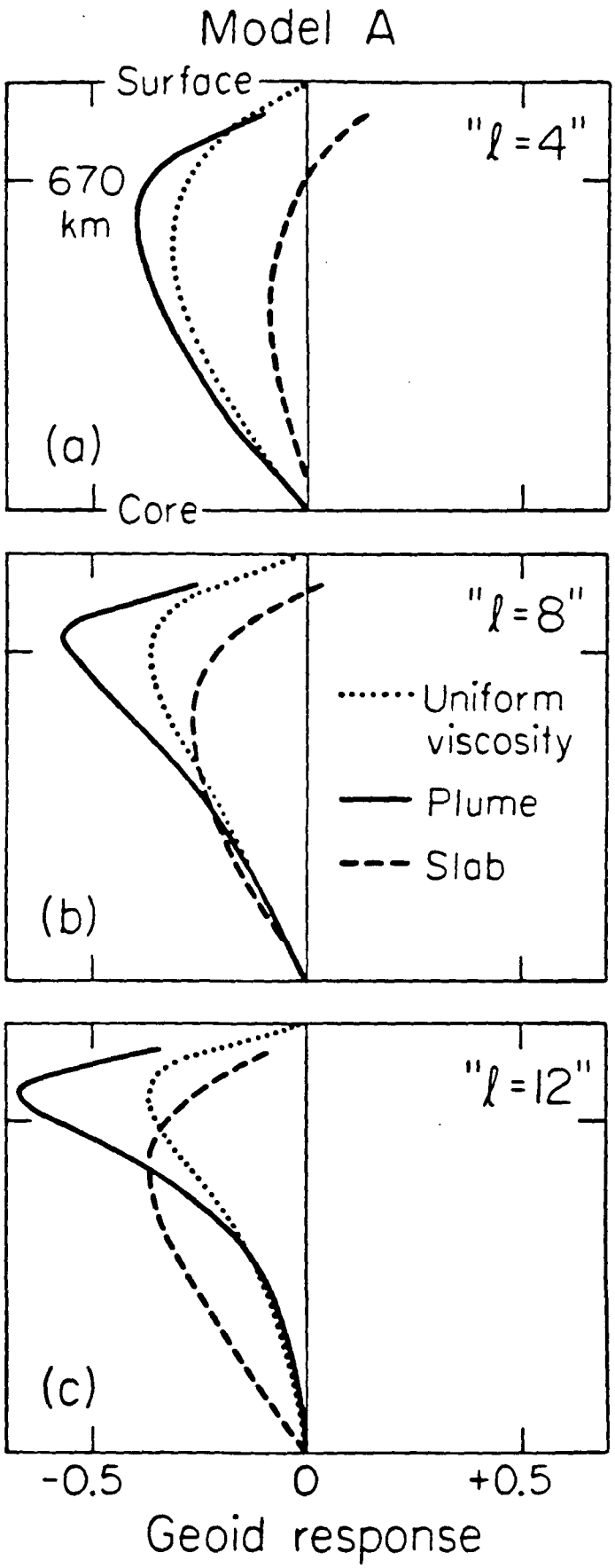
Model A
Surface
670
km
Core
(a)
"ℓ=4"
(b)
"ℓ=8"
Uniform
viscosity
Plume
Slab
(c)
"ℓ=12"
-0.5
0
+0.5
Geoid response

Figure 12

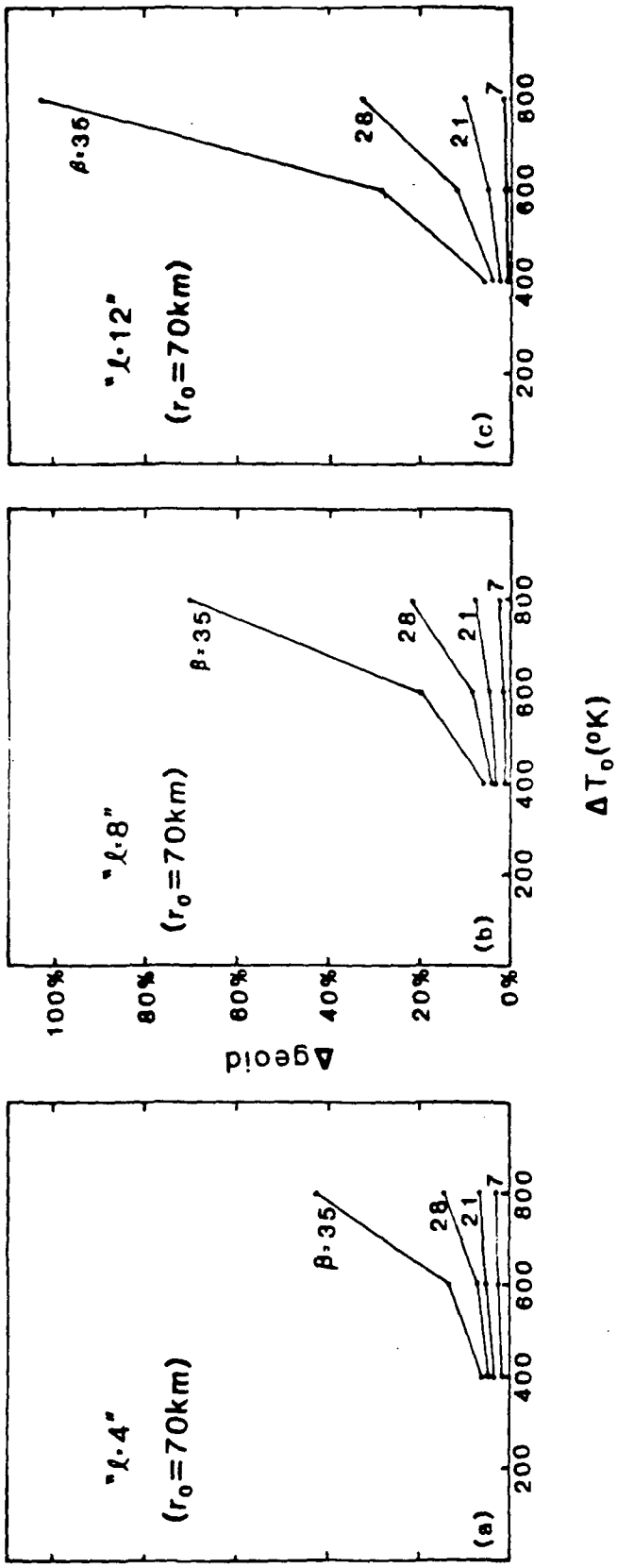
"ℓ·4"
(r_0=70km)
β·35
28
21
7
200
400
600
800
(a)
"ℓ·8"
(r_0=70km)
β·35
28
21
7
200
400
600
800
(b)
100%
80%
60%
40%
20%
0%
Δgeoid
"ℓ·12"
(r_0=70km)
β·36
28
21
7
200
400
600
800
(c)
ΔT$_0$(°K)

Figure 13

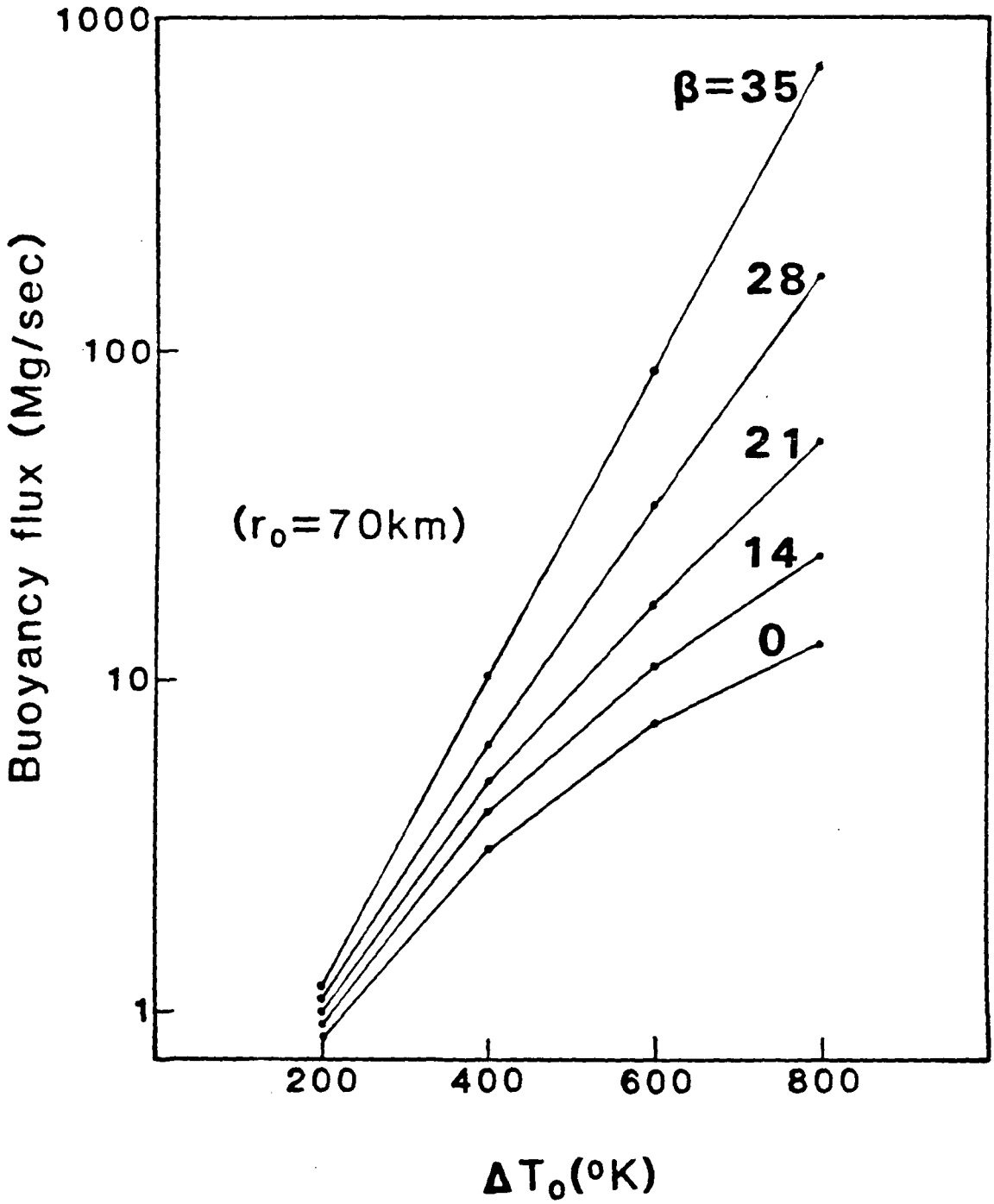
1000
100
10
1
Buoyancy flux (Mg/sec)
β=35
28
21
14
0
(r₀=70km)
200
400
600
800
ΔT₀(°K)

Figure 14

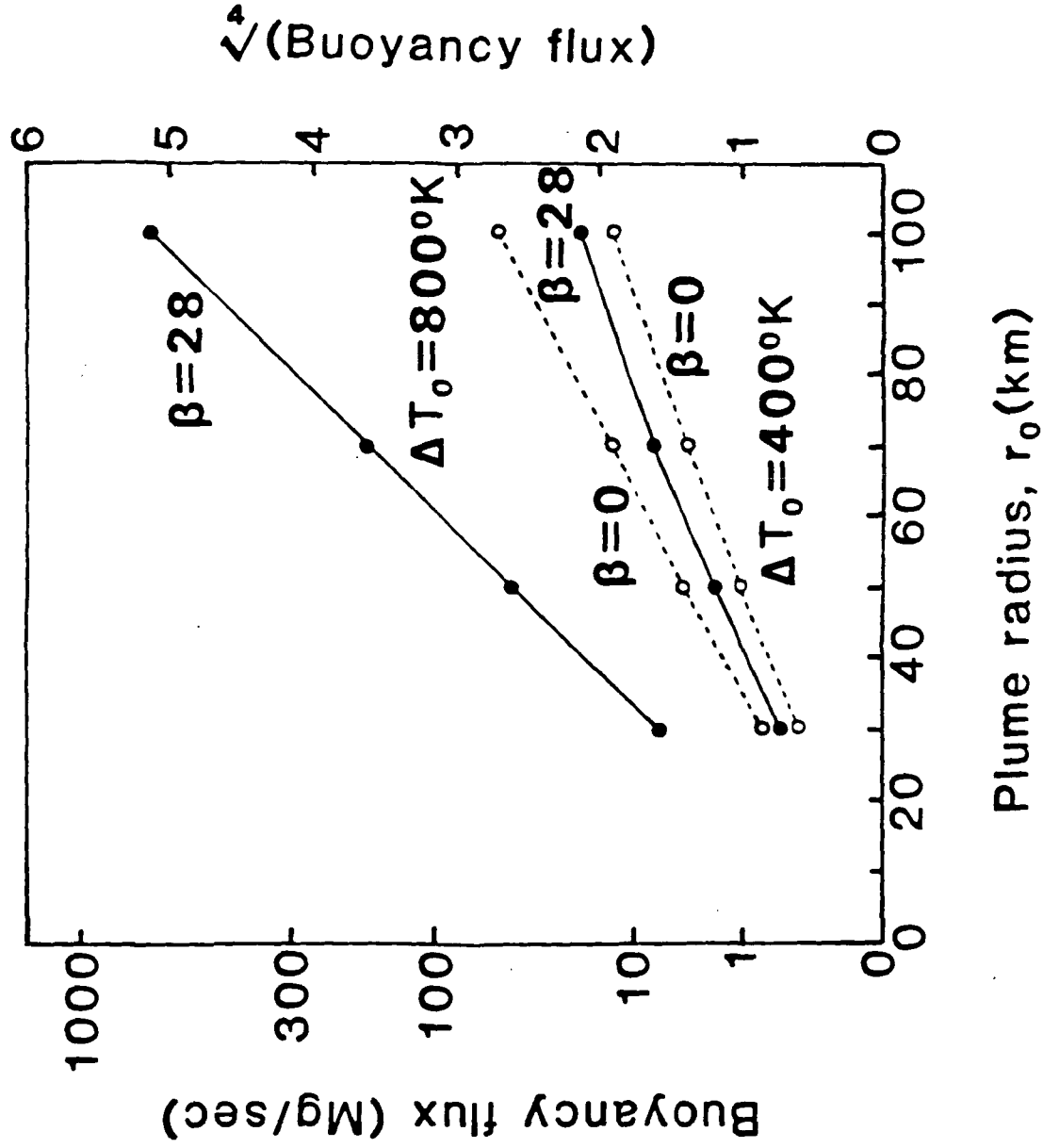
∜(Buoyancy flux)
6
5
4
3
2
1
0
β=28
ΔT₀=800°K
β=28
β=0
β=0
ΔT₀=400°K
1000
300
100
10
1
0
0
20
40
60
80
100
Buoyancy flux (Mg/sec)
Plume radius, r₀(km)

Figure 15

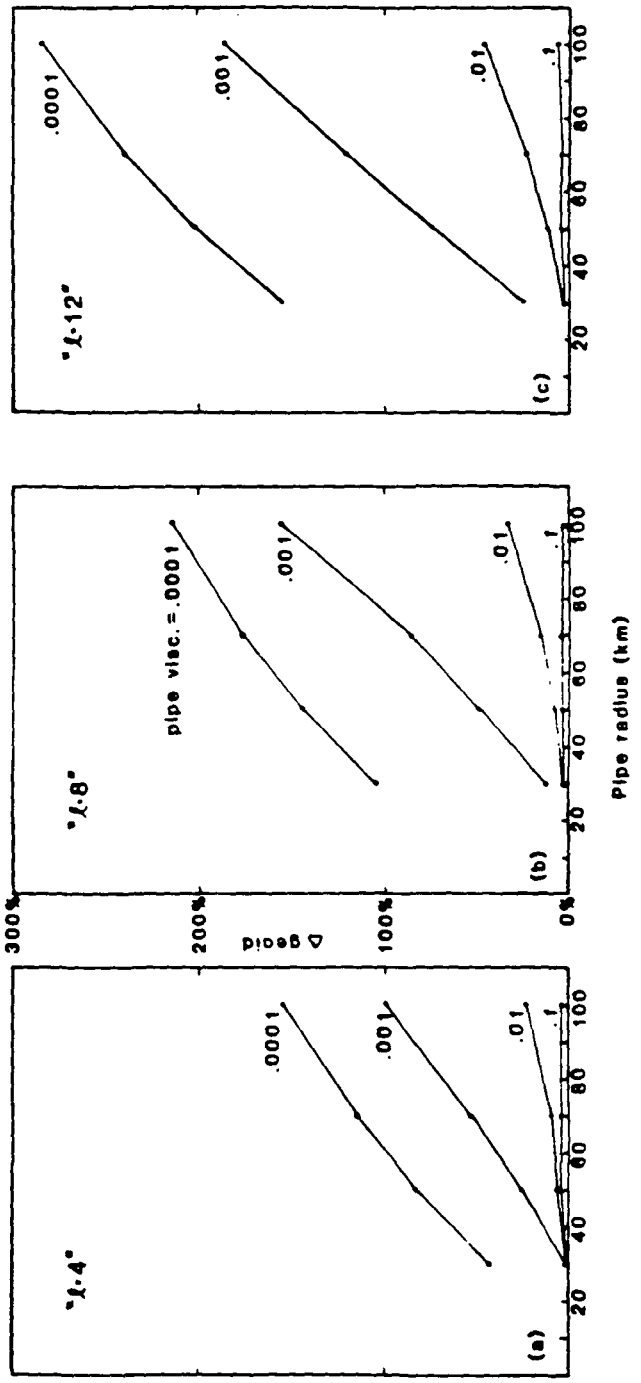
"1.4"
"1.8"
"1.12"
(a)
(b)
(c)
.0001
.001
.01
.1
1
pipe visc. = .0001
300%
200%
100%
0%
Δ geoid
20
40
60
80
100
Pipe radius (km)

Figure 16

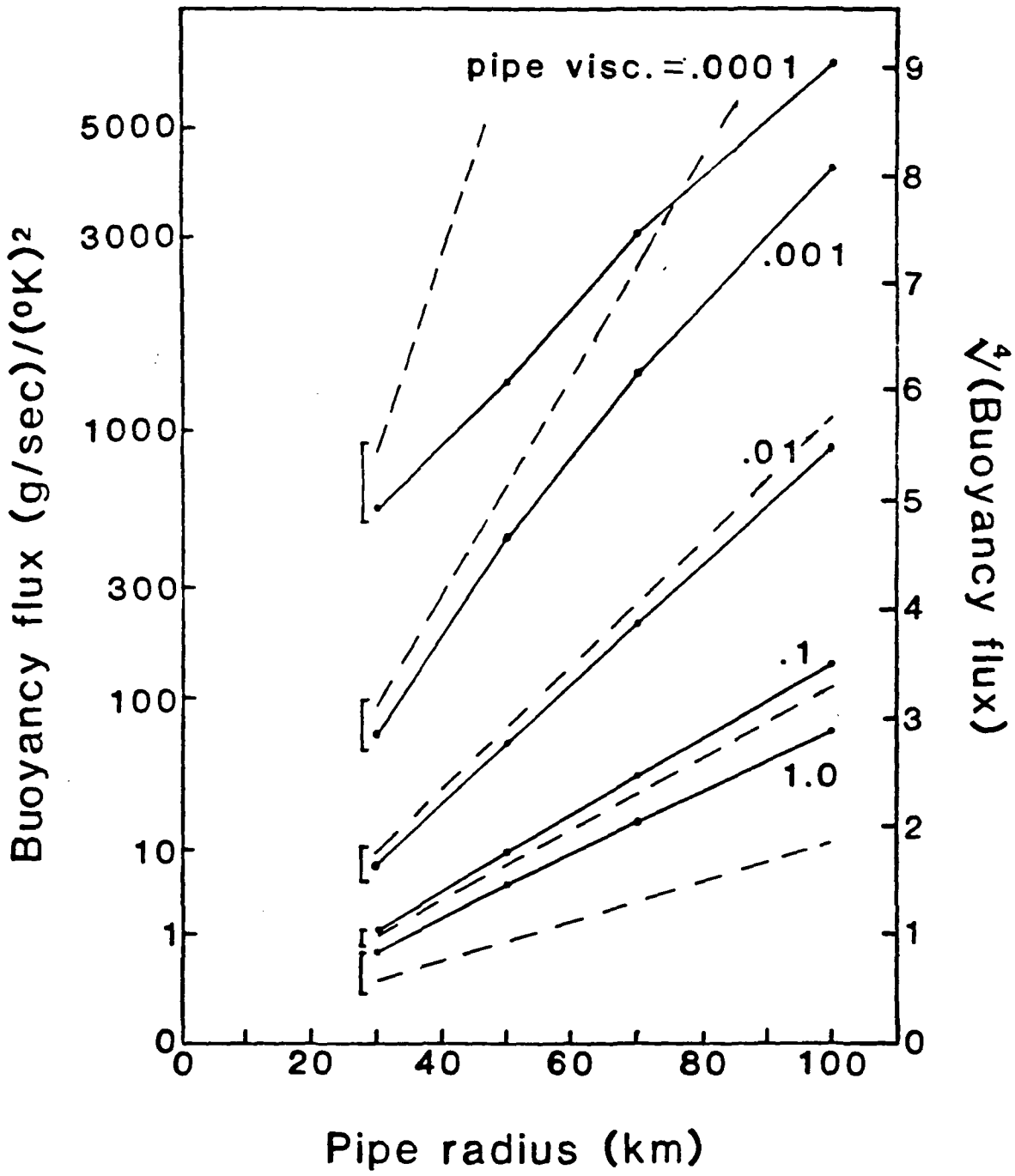
pipe visc. =.0001
.001
.01
.1
1.0
Buoyancy flux (g/sec)/(°K)²
∜(Buoyancy flux)
Pipe radius (km)
0
1
10
100
300
1000
3000
5000
0
20
40
60
80
100
0
1
2
3
4
5
6
7
8
9

Figure 17

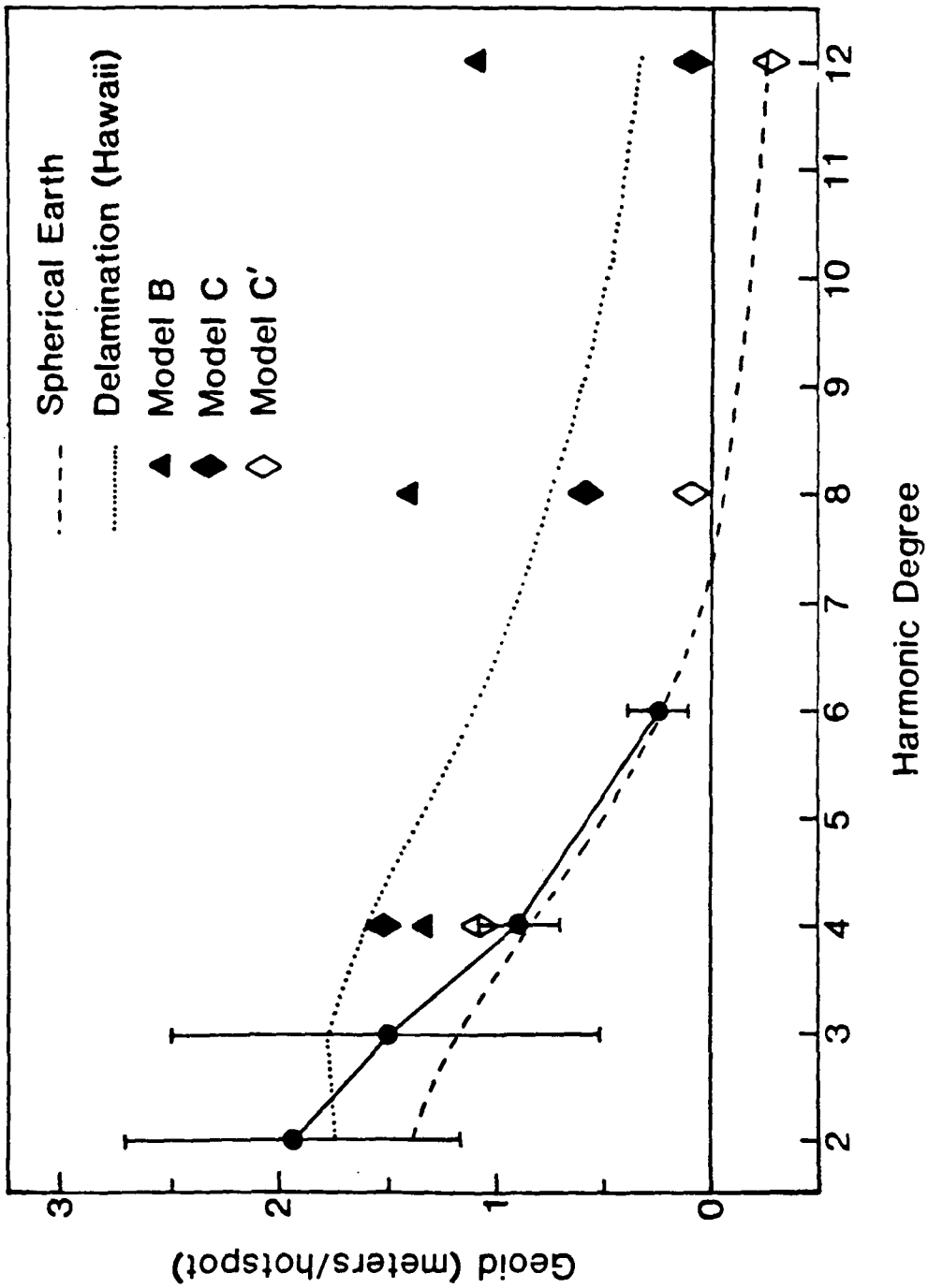
Spherical Earth
Delamination (Hawaii)
Model B
Model C
Model C'
Geoid (meters/hotspot)
Harmonic Degree
0
1
2
3
2
3
4
5
6
7
8
9
10
11
12

Figure 18

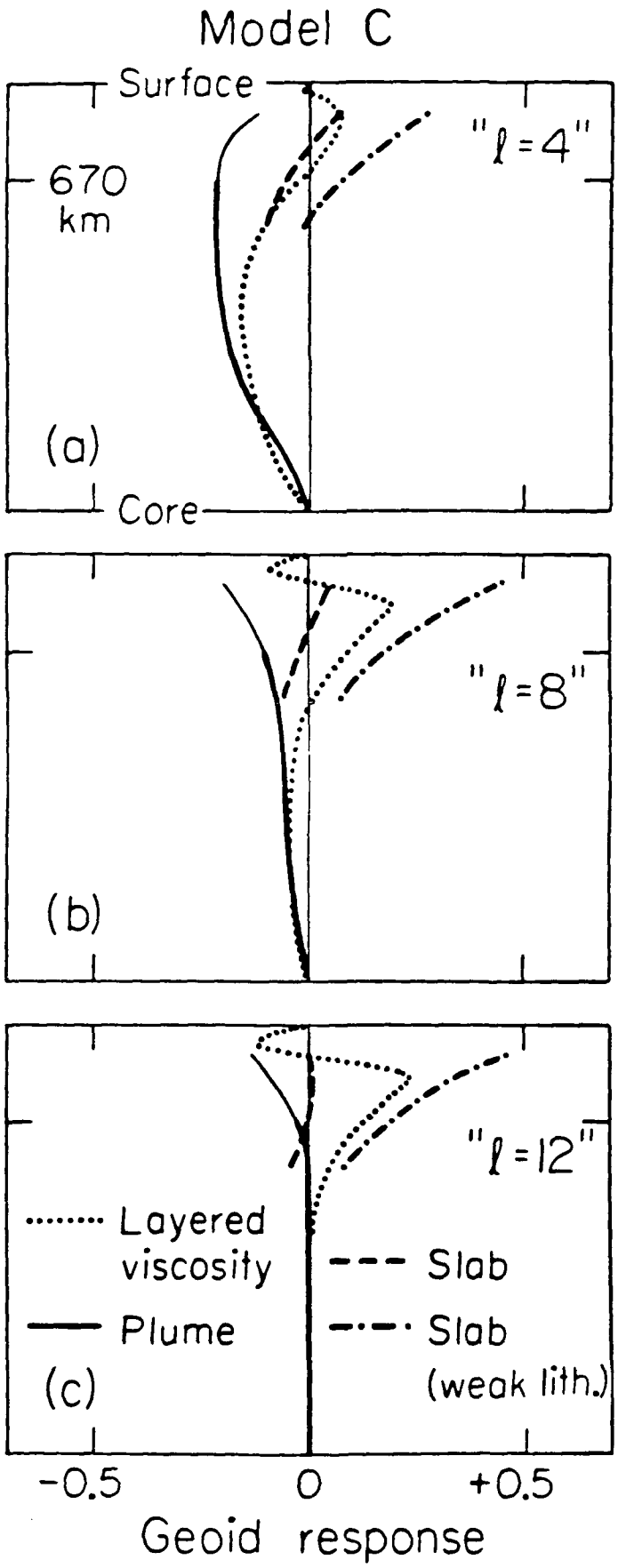
Model C
Surface
670
km
"l=4"
(a)
Core
"l=8"
(b)
"l=12"
Layered
viscosity
Plume
Slab
Slab
(weak lith.)
(c)
-0.5
0
+0.5
Geoid response

Figure 19

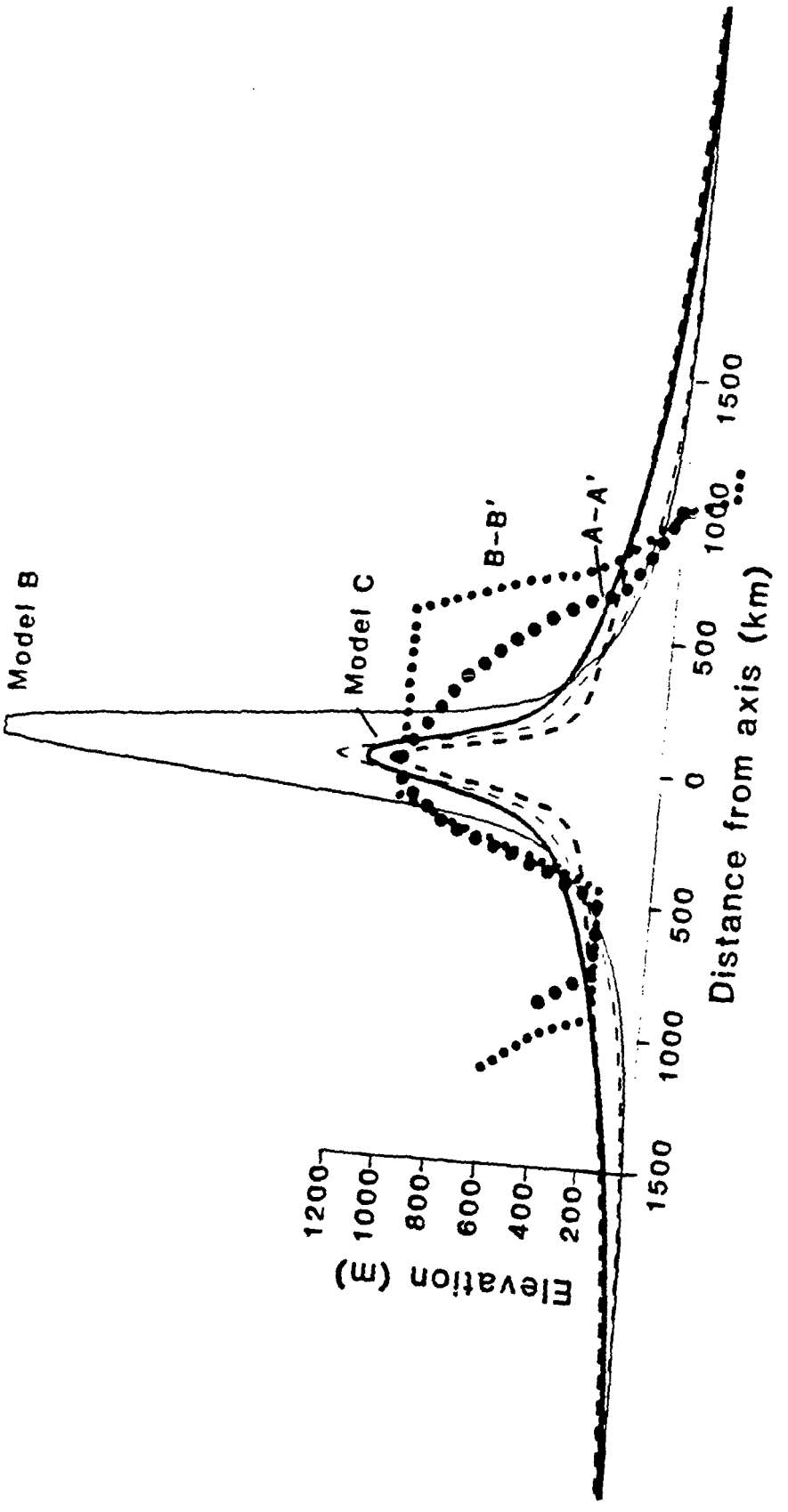
Model B
Model C
B-B'
A-A'
A
A'
Elevation (m)
1200
1000
800
600
400
200
1500
1000
500
0
500
1000
1500
Distance from axis (km)

Figure 20

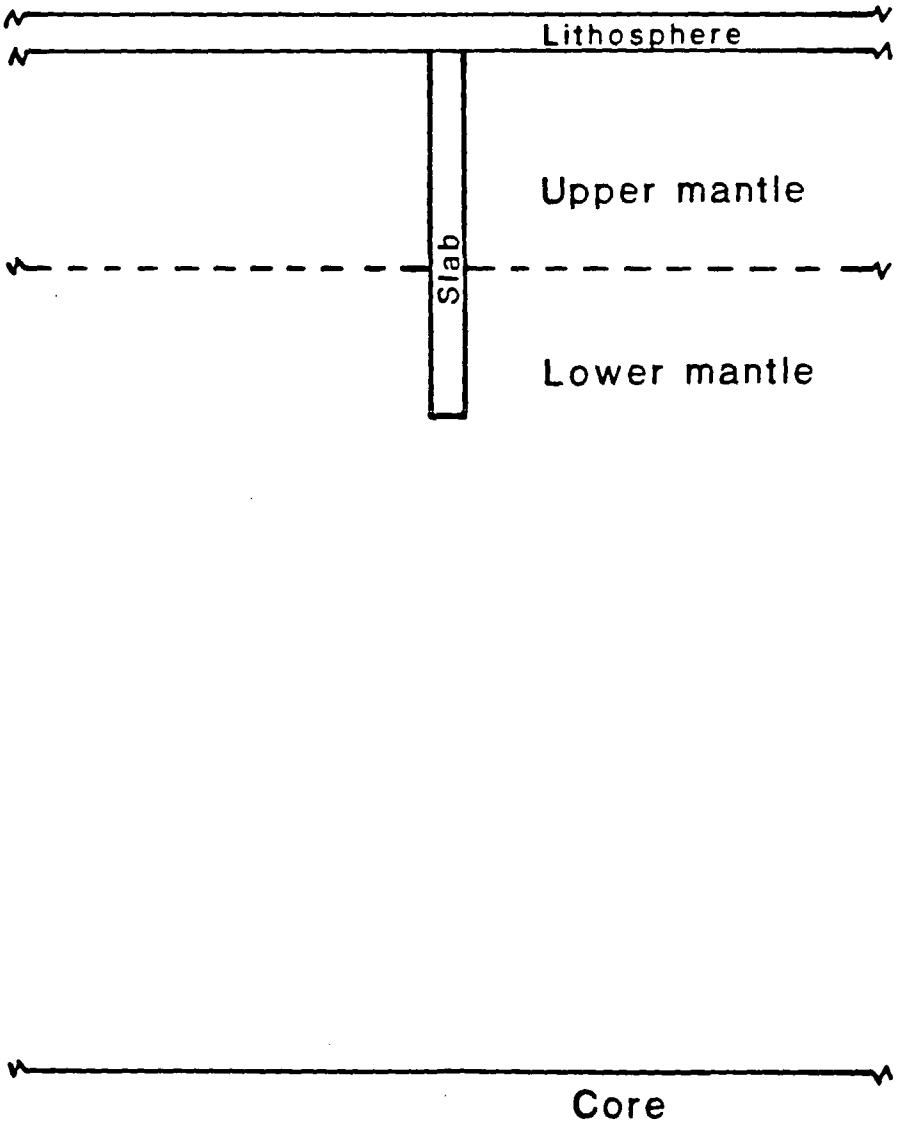

Figure B1

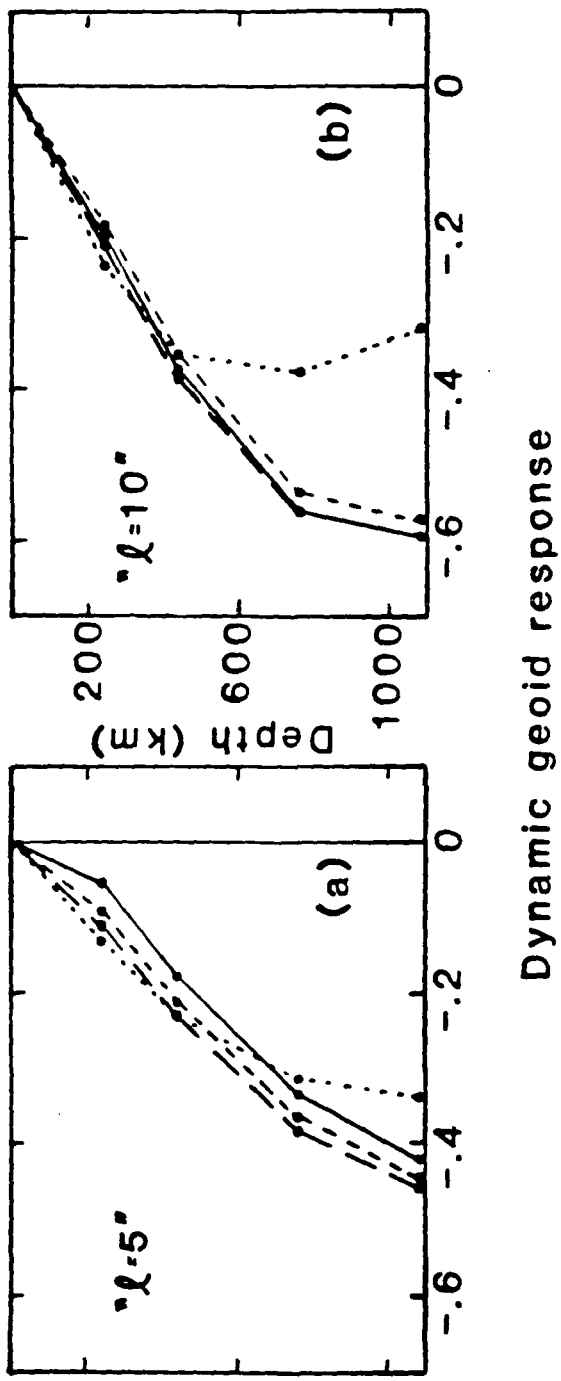

Figure B2

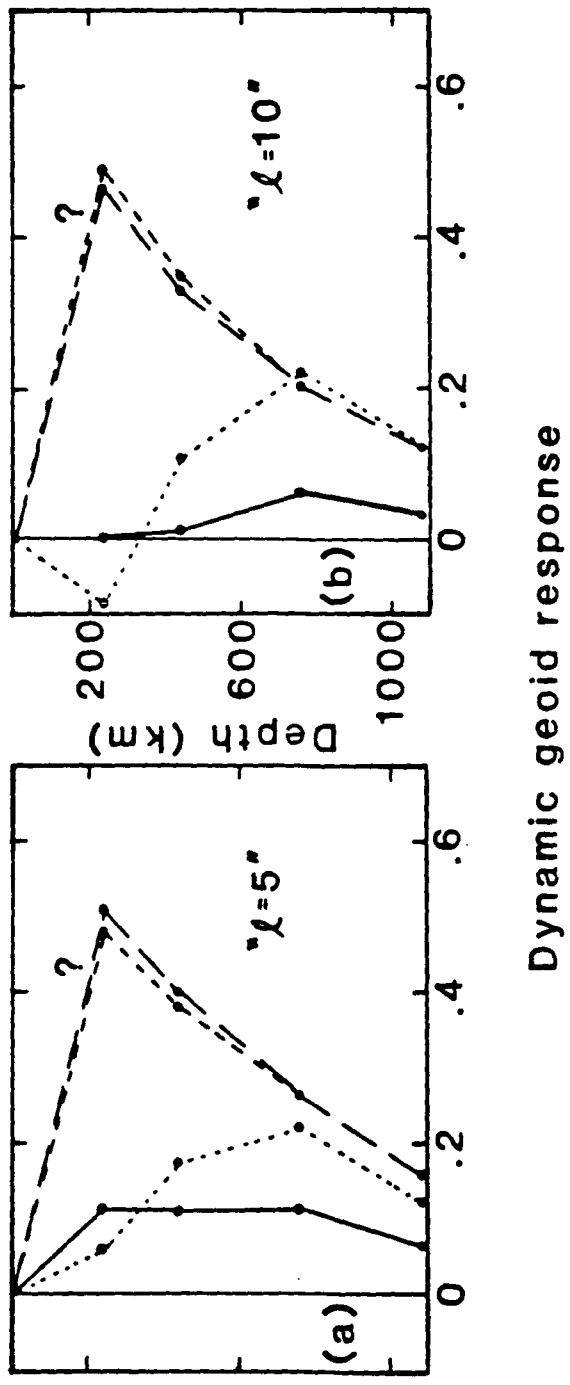

Figure B3